Department of Physics and Astronomy

University of Heidelberg

Bachelor Thesis in Physics

submitted by

Tim Arniko Meinhold

born in Bergisch Gladbach (Germany)

February 12th 1996

Stabilised laser-driven radiation pressure acceleration of ions

This Bachelor Thesis has been carried out by Tim Arniko Meinhold at the
Max Planck Institute for nuclear physics in Heidelberg
under the supervision of
Honorarprofessor Dr. Christoph H. Keitel

Stabilised laser-driven radiation pressure acceleration of ions

Abstract

The process of radiation pressure ion acceleration is investigated with the aim of suppressing the transverse Rayleigh-Taylor like interchange instabilities (RTI) in laser-foil interaction. This is achieved by imposing surface and density modulations on the target surface. First, calculations of the RTI growth rate are carried out in order to understand the behavior of the instabilities. Then, PIC (particle-in-cell) simulations of radiation pressure acceleration with different target modulation parameters are carried out. At the end, we analyze our simulation results and seek for optimal modulation parameters for a stabilized acceleration process of ions. It turned out that density modulated targets have more promising results than surface modulated targets and we get new findings in radiation pressure of ions which will probably lead to a new research direction.

Zusammenfassung

Die Beschleunigung durch Strahlungsdruck (RPA) von Ionen verursacht übertragbare Rayleigh-Taylor ähnliche Instabilitäten (RTI) im Innern von Laser-Plasma-Interaktionen. Diese RPA von Ionen bzw. die daraus folgende Wachstumsrate der transversalen Instabilitäten wird hier untersucht mit dem Ziel die RTI zu unterbinden bzw. zu dämpfen. Dies wird mit auferlegten Modulationen der Targetoberfläche erfolgen. Zuerst werden Rechnungen zu der RTI Wachstumsrate durchgeführt, um das Verhalten der Instabilitäten zu verstehen. Danach werden PIC (particle-in-cell) Simulationen des RPA Prozesses mit verschiedenen Parametern der Target-Modulationen durchgeführt. Schließlich werden die Simulations-Ergebnisse analysiert, und, wenn möglich, optimale Modulations-Parameter für einen stabilen Beschleunigungsprozess der Ionen ausgearbeitet. Es stellt sich heraus, dass Dichte-Modulationen vielversprechendere Ergebnisse erziehlen können als Oberflächen-Modulationen. Außerdem werden neue Erkenntnisse gefunden, die höchstwahrscheinlich zu einer neuen physikalichen Forschungsrichtung führen.

Table of Contents

1 Introduction

Radiation Pressure Acceleration (RPA) has often been used in astronomical physics before it was proposed to accelerate ions for tumour therapy [4, 8]. In fact, the mechanism with High-velocity Interstellar Photon Sails is based on the RPA of photons, that could accelerate nano-sensors up to 20% of light velocity within minutes [1]. The radiation pressure acceleration also has genesis in the studies of Einstein when Einstein studied the reflection of the a light from a mirror and deduced that the ratio E/ω, where E is the electric field and ω is the frequency of the light, is an invariant which later turns out to be the Planck constant ($E_p = h\nu = hc/\lambda$). Since the first proposed concept of ion RPA [2], theses mechanisms have been studied over the past years. With super-intense polarized lasers around $10^{23}\,\mathrm{W/cm^2}$, RPA have the potential to produce high-energy ion beams with higher energy conversation efficiency compared to lower laser intensity mechanisms like target normal sheath acceleration (TNSA). RPA of ions promises to provide ultrashort pulse duration, extremely high peak energy having a great potential in ion beam therapy [3–9] or in other physical areas like fast ignition [10–13].

Seeking a stabilized RPA of ions has been a long-standing goal in this research area. In fact, transverse instabilities in high-power laser-plasma interaction reduce the effectiveness, restrain or even break the RPA process. This mechanism has been studied over the past decades and a several attempts like analysis of the intrinsic instability origin [14], tailored electromagnetic pulses with sharp intensities [15] or modulation of the RPA [16] tried to suppress the instabilities.

In order to suppress the RTI, we will use a modulated target with different shapes. The major difference to [17] is, that we will make different modulations, target shapes, and compare it with the growth of RTI instabilities in each case. Finally, we see some results on the effect of considering the radiation reaction process for the most promising cases (see the Outlook).

2 Theoretical Background

2.1 Choosing the right setting for the RPA

2.1.1 Polarization of the laser

The polarization of the laser is significant for RPA of ions. In fact, a linear polarized laser will have higher electron heating than those with circular polarized lasers [18], and consequently the RPA is weaker for the linearly polarized case. Laser polarization allows a phase stable region for the RPA mechanism. This is due to the ponderomotive force *i.e* $\boldsymbol{v} \times \boldsymbol{B}$ force, which is zero for circular polarization. For this reason we use circular polarized lasers in this research project. In this case, the radiation pressure force will apply a constant pressure to the target shell which starts accelerating the high plasma density layer. For target widths $\ell < (a_0 n_c/\pi n_e)\lambda_0$ (where a_0 is the dimensionless laser amplitude, λ_0 is the laser wavelength, n_e the electron density and n_c the critical plasma density), the laser pushes the plasma surface into the target. This happens as long as the laser pulse continues and therefore, there is no density limit for the target. This is also called the hole boring regime (HB). In our case, we will focus on much thinner targets (thickness around laser wavelength) and higher laser intensities up to $I_{cp} = 1.71 \times 10^{23}\,\mathrm{W/cm^2}$ *i.e* light sailing regime (LS). Instead of a laser push of the plasma into the target, the target starts moving in the forward direction.

2.1.2 Intensity of the laser

The intensity of the laser is very important as it plays a major role in the energy gaining process. For lasers beyond (10^{23} W/cm^2), the ions become relativistic and the system will generate much higher energy. For lower intensities and thick targets, the target normal sheath acceleration (TNSA) dominates. The laser heats up the electrons at the front of the target and and these hot-electrons start re-circulating

inside the target. Due to this a charge separation electric field is generated at the back of the target which accelerates the ions. But as a matter of fact, the ion energy is only proportional to the square root of the laser power. In the opposite way, for thinner targets and higher laser intensities, one can get the Coulomb explosion regime (CE). Here are the target electrons mostly expelled from the front surface and the ions 'explode' due to the remaining positive charge. The ion energy is here proportional to the laser power. For our case, we will use the RPA mechanism, as for high laser intensities, there is sufficient energy to push the foil as a whole and it has a high efficiency in the ultra-relativistic regime. In principle, the target gets almost all the laser energy which leads to high-energy ion beams with higher energy conversation efficiency.

2.1.3 Surface density and other parameters of the target

For the stability of a thin foil undergoing acceleration, perturbations with wavelength higher than the target width, are to be avoided. We here employ the competitive feeding of the instability modes. If one modulates the target surface at a given wavelength, then one feeds this particular mode of the instability compared to others. Thus the free energy of the plasma is diverted to this mode and one can hope to suppress modes at other wavelengths, especially the modes which are detrimental for the target stability *e.g* the modes with wavelengths of the order of target thickness. We study this selective mode feeding for different target shapes and modulations (see section 3) and compared them with a flat target case.

In our case, we will use a maximum density of

$$n = 250\, n_c = 250 \cdot \frac{\omega_0^2 m_e}{4\pi e^2},$$

$$n = 4.36 \times 10^{23}/\mathrm{cm}^3, \tag{0a}$$

where n_c is the critical density for the laser pulse for ($1\,\mu$m) laser wavelength and $\omega_0 = 2.36\times10^{15}$/s is the laser frequency for Ti:Sa lasers which operate most efficiently at wavelengths near 0.8×10^{-6} m.

The density threshold is linked to the laser intensity with a dimensionless parameter

$$\epsilon_p \geq a_0, \tag{0b}$$

where a_0 is the dimensionless amplitude of the laser (definition below) and $\epsilon_p = \pi n_e \ell / n_c \lambda_0$, where n_e is the electron density, ℓ the target width, n_c the critical density and λ_0 the laser wavelength. In our case, we want to be in the light sailing regime, which is $a_0 > \pi$ for a $1\lambda_0$ thick target and $a_0 > 2\pi$ for a $2\lambda_0$ thick target.

The normalized dimensionless Lorentz invariant amplitude of the laser electric field is

$$a_0 = \frac{eE_0}{m_e \omega_0 c}, \tag{0c}$$

where E_0 is the initial energy of the laser, e the electron charge, c the speed of light and m_e the electron mass. $a_0 = 150$ corresponds to a circular polarized laser intensity of $I_{cp} = 6.16 \cdot 10^{22}\,\mathrm{W/cm^2}$. Later on, one can consider the value of $a_0 = 250$ (*i.e* $I_{cp} = 1.71 \cdot 10^{23}\,\mathrm{W/cm^2}$) where radiation reaction has to be considered. Please note, that the two values of a_0 validate the inequality (0b).

2.2 Determination of the growth rate of the RTI

2.2.1 Defining the system

For the RPA of a thin flat target, we define a system with a constant electromagnetic field for the laser, a thickness l_0 of the flat target, the surface of the flat target $\mathrm{d}S_0$ and a velocity ν_0 of the target at time $t = 0$. As known from theory, the RPA is coming from the velocity of the photons (momentum of the electromagnetic wave) and from their reflection. The so called hot electrons excited by the momentum of

the photons, transport the absorbed energy

$$\mathcal{E}_p = m_e c^2(\gamma - 1) = m_e c^2(\sqrt{1 + {a_0}^2/2} - 1), \tag{1}$$

with a_0 the dimensionless amplitude of the laser, m_e the electron mass and c the velocity of light. This energy is also known as the ponderomotive energy. The ions are accelerated by the radiation pressure which will overcome the charge separation force. As a matter of fact, we know *e.g* that with $\mathcal{E}_p = 500\,\mathrm{MeV}$, $m_e c^2 = 0.5\,\mathrm{MeV}$ and $m_i c^2 = 1000\,\mathrm{MeV}$, we can estimate the ion velocity with $\gamma_i = 1.5,\ \gamma_e \approx 1000$ and therefore $\nu_i \approx 0.7c$ and $\nu_e \approx c$ are the respective velocities of the ions and electrons.

At a time t, the shape of the flat target can be curved as the velocity of the target is not equal in space. We define therefore a new thickness l and new surface $\mathrm{d}S$ of the target, both dependent in time. We can then describe the shell shape of the system in dependence of time as follow

$$\vec{M} = \vec{M}(\zeta, \eta, t) = \{x(\zeta, \eta, t),\ y(\zeta, \eta, t),\ z(\zeta, \eta, t)\}, \tag{2}$$

where (ξ, ζ, η) is a set of orthogonal curvilinear coordinates to describe the evolution of a differential element of the thin-foil element after the laser hits the target. The shell's evolution is described by the function $\vec{M}(\zeta, \eta, t)$. The equation of motion for the mass-limited target, driven by the radiation pressure is then written as

$$\frac{\mathrm{d}\vec{p}}{\mathrm{d}t} = \frac{\mathcal{P}\vec{n}}{\sigma}, \tag{3}$$

where $\mathcal{P}$ is the relativistically invariant radiation pressure, $\vec{p}$ the momentum of the shell, $\vec{n}$ the unit vector normal to the surface and $\sigma = ln$ the surface density of the shell where n is the total number of particles in the shell.

The mass of the shell does not change in time and is $\mathrm{d}m = \sigma\,\mathrm{d}\zeta\mathrm{d}\eta$ for all times t. This can be explained by the fact that the total number of particles does not change and $n = n_0$. Therefore, at a regular point, we have following the equation

$$|\mathrm{d}\sigma| \cdot \sigma = |\mathrm{d}\sigma_0| \cdot \sigma_0, \tag{4}$$

and the differential area $\mathrm{d}\sigma$ changes for any regular point with vector $\vec{r}$ as

$$|\mathrm{d}\sigma| = \left|\frac{\mathrm{d}\vec{r}}{\mathrm{d}\zeta} \times \frac{\mathrm{d}\vec{r}}{\mathrm{d}\eta}\right| \mathrm{d}\zeta\mathrm{d}\eta. \tag{5}$$

The surface mass density at any time is therefore

$$\sigma = \sigma_0 \left|\frac{\mathrm{d}\vec{r}}{\mathrm{d}\zeta} \times \frac{\mathrm{d}\vec{r}}{\mathrm{d}\eta}\right|^{-1}, \tag{6}$$

where only the stretching in transverse directions is considered and hence

$$\begin{aligned} \frac{\sigma}{\sigma_0} &= \left|\frac{\mathrm{d}\vec{r}}{\mathrm{d}\zeta} \times \frac{\mathrm{d}\vec{r}}{\mathrm{d}\eta}\right|^{-1}, \\ \frac{\sigma}{\sigma_0} &= \left[\{y,z\}^2 + \{z,x\}^2 + \{x,y\}^2\right]^{-1/2}, \end{aligned} \tag{7}$$

where the Poisson brackets are defined as

$$\{x_i, x_k\} = \frac{\partial x_j}{\partial\zeta}\frac{\partial x_k}{\partial\eta} - \frac{\partial x_k}{\partial\zeta}\frac{\partial x_j}{\partial\eta}. \tag{8}$$

The equation of motion (3) can therefore be rewritten as

$$\frac{\mathrm{d}p_i}{\mathrm{d}t} = \frac{\mathcal{P}}{\sigma_0}\,\epsilon_{ijk}\,\partial_\zeta x_j\,\partial_\eta x_k, \tag{9}$$

where ϵ_{ijk} is the anti-symmetric Levi-Civita tensor, $\partial_\zeta = \partial/\partial\zeta$ (analog for η), $\{x_i\} = \{x, y, z\}$ and $\{p_i\} = \{p_x, p_y, p_z\}$. Hence, the components of equation of motion (9)

can be expressed as

$$\frac{\mathrm{d}p_x}{\mathrm{d}t} = \frac{\mathcal{P}}{\sigma_0}\,\left[\,\partial_\zeta y\,\partial_\eta z - \partial_\eta y\,\partial_\zeta z\,\right], \tag{10a}$$

$$\frac{\mathrm{d}p_y}{\mathrm{d}t} = \frac{\mathcal{P}}{\sigma_0}\,\left[\,\partial_\zeta z\,\partial_\eta x - \partial_\zeta x\,\partial_\eta z\,\right], \tag{10b}$$

$$\frac{\mathrm{d}p_z}{\mathrm{d}t} = \frac{\mathcal{P}}{\sigma_0}\,\left[\,\partial_\zeta x\,\partial_\eta y - \partial_\eta x\,\partial_\zeta y\,\right]. \tag{10c}$$

The relativistically invariant radiation Pressure $\mathcal{P}$, which can be calculated with the Maxwell stress-energy tensor, is needed. Its diagonal or rather Maxwell stress tensors' diagonal elements will provide the pressure respectively the expression of $\mathcal{P}$. The electromagnetic stress-energy tensor is:

$$T^{\mu\nu} = \frac{\partial\mathcal{L}}{\partial(\partial_\mu A_\rho)}\,\partial^\nu A_\rho - g^{\mu\nu}\mathcal{L} = \frac{1}{4\pi}F^{\rho\mu}\partial^\mu A_\rho - g^{\mu\nu}\mathcal{L},$$

$$T^{\mu\nu} = \frac{1}{4\pi}\left(F^{\mu\rho}F^{\nu}_{\rho} - \frac{1}{4}g^{\mu\nu}F_{\sigma\rho}F^{\sigma\rho}\right), \tag{11}$$

where $\mathcal{L}$ is the Lagrangian function, A is the four-potential, $F_{\mu\nu}$ the electromagnetic field tensor and $g^{\mu\nu}$ the reciprocal of the metric tensor. The diagonal elements of the Maxwell stress-energy tensor $T_{mn} = -\sigma_{mn}$ (with $m = n$), have a negative sign included. That's why the diagonal elements of the Cauchy stress tensor are

$$\sigma_{nn} = \frac{1}{4\pi}\left(E_n^2 + B_n^2 - \frac{1}{2}\left(E^2 + B^2\right)\right). \tag{12}$$

Knowing that the frequency of the reflected electromagnetic wave is reduced [19] by $(1-\beta_x)/(1+\beta_x) \approx 1/(4\gamma^2)$, with $\gamma = (1-{\beta_x}^2)^{-1/2}$ and $\beta_x = v_x/c = p_x/\sqrt{{m_i}^2c^2 + {p_k}^2}$ (v_x, the longitudinal velocity of the shell, m_i the ion mass, c the speed of light and p_k the momentum vector with $k = \{x, y, z\}$), the energy of the

reflected electromagnetic pulse is then

$$E_r = E_0 \sqrt{\frac{1-\beta_x}{1+\beta_x}}, \tag{13}$$

with E_0 the initial energy of the laser.

Therefore, with equations (12) and (13), the relativistically invariant radiation pressure is

$$\mathcal{P} = k\frac{{E_0}^2}{4\pi}\frac{1-\beta_x}{1+\beta_x} = \frac{{E_0}^2}{2\pi}\frac{1-\beta_x}{1+\beta_x}, \tag{14}$$

where $k = 2|\rho|^2 + |\alpha|^2$ with $|\rho|^2$ and $|\alpha|^2$ are the reflection and absorption coefficients, respectively. In this case, the shell is an ideally reflective target and $k = 2$.

2.2.2 Interchange instability: Solving the equilibrium of motion

To know the behaviour of the instability, one can solve at first the equilibrium of motion of the unperturbed shell. At $t = 0$, the initial conditions are $x_0 = 0,\ y = \zeta,\ z = \eta$. The perturbations of the initial conditions are denoted as $\delta x\,(\phi, \zeta, \eta),\ \delta y\,(\phi, \zeta, \eta),\ \delta z\,(\phi, \zeta, \eta)$. They are first solved for the equilibrium motion in x-direction. To find out the growth rate of the RTI, we perturb later on this equilibrium.

We define now the phase of the wave φ as

$$\varphi = \omega_0 \left[t - \frac{x_0(t)}{c} \right], \tag{15}$$

where $x_0(t)$ is the unperturbed position of the shell. The energy is hence

$$E_0 = E \left[t - \frac{x_0(t)}{c} \right]. \tag{16}$$

Differentiating equation (15) with respect to time, we get

$$\frac{\mathrm{d}\varphi}{\mathrm{d}t} = \omega_0 \left[1 - \frac{\dot{x}_0(t)}{c}\right],$$
$$\frac{\mathrm{d}\varphi}{\mathrm{d}t} = \omega_0 \frac{m_i c\gamma_0 - p_x^0}{m_i c\gamma_0}, \tag{17}$$

where $p_x^0 = m_i\,\gamma_0\,v_x^0$ is the momentum of the shell.

We can therefore write equation (10a) as

$$\frac{\mathrm{d}p_x^0}{\mathrm{d}t} = \frac{E_0^2}{2\pi\sigma_0}\,\frac{m_i c\gamma_0 - p_x^0}{m_i c\gamma_0 + p_x^0}. \tag{18}$$

Using the equation of the phase variable (17) one can get

$$\frac{\mathrm{d}p_x^0}{\mathrm{d}\varphi} = \frac{E_0^2}{2\pi\sigma_0\omega_0}\,\frac{m_i c\gamma_0}{m_i c\gamma_0 + p_x^0}. \tag{19}$$

We define the normalized fluence of the laser pulse (energy iterating over time) as

$$W(\varphi) = \int_0^{\varphi} \frac{R(\varphi')}{\lambda_0}\,\mathrm{d}\varphi', \tag{20}$$

where $R(\varphi) = E_0^2(\varphi)/(m_i\sigma_0\omega_0^2)$ and $\lambda_0 = 2\pi c/\omega_0$

Integrating equation (19) yields to

$$\int_0^{p_x^0} \mathrm{d}p_x^0 \frac{(m_i c\gamma_0 + p_x^0)}{m_i c\gamma_0} \cdot \frac{1}{m_i c} = \int_0^{\varphi} \frac{E_0^2(\varphi)}{2\pi\sigma_0\omega_0} \cdot \frac{\omega_0}{\omega_0 m_i c}\,\mathrm{d}\varphi,$$
$$\frac{1}{m_i c}\int_0^{p_x^0} \mathrm{d}p_x^0 \left(1 + \frac{p_x^0}{m_i c\gamma_0}\right) = \int_0^{\varphi} \frac{R(\varphi)}{\lambda_0}\,\mathrm{d}\varphi,$$
$$\frac{1}{m_i c}\int_0^{p_x^0} \mathrm{d}p_x^0 + \int_0^{p_x^0} \frac{p_x^0\,\mathrm{d}p_x^0}{\sqrt{m_i^2 c^2 + p_x^{0\,2}}} = W(\varphi),$$

$$p_x^0 + \sqrt{{p_x^0}^2 + (m_i c)^2} - m_i c = m_i c\, W(\varphi),$$

$${p_x^0}^2 + (m_i c)^2 = (m_i c\,(W(\varphi)+1) - p_x^0)^2,$$

$${p_x^0}^2 + (m_i c)^2 = [(W(\varphi)+1)m_i c]^2 + {p_x^0}^2 - 2p_x^0(W(\varphi)+1)m_i c,$$

$$p_x^0 = -\frac{{p_x^0}^2 - p_x^0 + (m_i c)^2 - [(W(\varphi)+1)m_i c]^2}{2(W(\varphi)+1)m_i c},$$

$$p_x^0 = m_i c\,\frac{[W(\varphi)+1]^2 - 1}{2(W(\varphi)+1)},$$

$$\boxed{p_x^0 = m_i c\,\frac{W(\varphi)[W(\varphi)+2]}{2(W(\varphi)+1)}.} \tag{21}$$

This is the solution of equation (18) where the initial condition is $p_x^0(0) = 0$.

In order to analyze the instabilities, we evaluate the quantities around the equilibrium values. To get the linearized equation, p_x^0 is linerized first. We have following equations for $\vec{p}$ and $\vec{\beta}$:

$$\frac{{p_x^0}^2}{m_i^2 c^2} = \frac{\beta_x^2}{1-\beta_x^2},$$
$$\frac{p_x^0}{m_i c} = \frac{\beta_x}{(1-\beta_x^2)^{1/2}}, \tag{22}$$

$$\vec{p} = (p_x^0 + \delta p_x)\hat{x} + \delta p_y\,\hat{y} + \delta p_z \hat{z}, \qquad \vec{\beta} = (\beta_x^0 + \delta\beta_x)\hat{x} + \delta\beta_y\,\hat{y} + \delta\beta_z\hat{z}. \tag{23}$$

Here are $\beta_y^0 = \beta_z^0 = 0$. Furthermore, one calculates p_x in some steps:

$$1 - \beta_x^2 = 1 - (\beta_x^2 + 2\delta\beta_x\beta_x^0) = (1 - {\beta_x^0}^2)\left[1 - \frac{2\delta\beta_x\beta_x^0}{1-{\beta_x^0}^2}\right],$$

$$\sqrt{1-\beta_x^2} = \sqrt{1-{\beta_x^0}^2}\left[1 - \frac{2\delta\beta_x\beta_x^0}{1-{\beta_x^0}^2}\right]^{1/2} = \sqrt{1-{\beta_x^0}^2}\left[1 - \frac{\delta\beta_x\beta_x^0}{1-{\beta_x^0}^2}\right],$$

$$\frac{\beta_x}{\sqrt{1-\beta_x^2}} = \frac{\beta_x^0 + \delta\beta_x}{\sqrt{1-\beta_x^{0\,2}}\left[1-\frac{\delta\beta_x\beta_x^0}{1-\beta_x^{0\,2}}\right]},$$

$$\frac{\beta_x}{\sqrt{1-\beta_x^2}} = \gamma_0\beta_x^0\left(1+\frac{\delta\beta_x}{\beta_x^0}\right)\left[1+\frac{\delta\beta_x\beta_x^0}{1-\beta_x^{0\,2}}\right],$$

$$\frac{\beta_x}{\sqrt{1-\beta_x^2}} = \gamma_0\beta_x^0(1+0)\left[1+\delta\beta_x\beta_x^0\gamma_0^2\right],$$

$$\frac{p_x}{m_i c} = \gamma_0\beta_x^0 + \delta\beta_x\,\beta_x^{0\,2}\gamma_0^3.$$

Hence

$$p_x = p_x^0 + m_i c\,\gamma_0^3\,\beta_x^{0\,2}\,\delta\beta_x. \tag{24a}$$

One can analogically write

$$p_y = m_i c\,\gamma_0\,\delta\beta_y, \tag{24b}$$

$$p_z = m_i c\,\gamma_0\,\delta\beta_z. \tag{24c}$$

Since $\varphi = \omega_0\,[t\,-\,x_0(t)/c]$ yields to $\partial_t\varphi = \omega_0\,[t\,-\,\beta_x^0(t)/c] \approx \omega_0/2\gamma_0^2 \approx \omega_0 m_i^2 c^2/2p_x^{0\,2}$ in the ultra-relativistic limit, and $\partial_t = \partial_\varphi\,\partial_t\varphi$, one can get

$$\frac{\partial\delta x}{\partial t} = \frac{\partial\delta x}{\partial\varphi}\,\frac{\partial\varphi}{\partial t} = \frac{\omega_0 m_i^2 c^2}{2p_x^{0\,2}}\,\frac{\partial\delta x}{\partial\varphi}. \tag{25}$$

Solving equations (10a), (10b) and (10c) for the initial conditions

$$x = 0 + \delta x, \qquad y = \zeta + \delta y, \qquad z = \eta + \delta z,$$

one gets

$$\frac{\mathrm{d}p_x}{\mathrm{d}\varphi} = \frac{E_0^2 m_i c\gamma_0}{2\pi\sigma_0\omega_0(m_i c\gamma_0 + p_x^0)}\left[1+\frac{\partial\delta y}{\partial\zeta}+\frac{\partial\delta z}{\partial\eta}\right]. \tag{26}$$

And then,

$$\frac{\mathrm{d}p_x^0}{\mathrm{d}\varphi} = \frac{E_0^2 m_i c\gamma_0}{2\pi\sigma_0\omega_0(m_i c\gamma_0 + p_x^0)},$$

$$\frac{\partial}{\partial\varphi}\left[m_i c\beta_x^{0^2}\gamma^3\,\frac{\delta\dot{x}}{c}\right] = \frac{E_0^2 m_i c\gamma_0}{2\pi\sigma_0\omega_0(m_i c\gamma_0 + p_x^0)}\,\left[\frac{\partial\delta y}{\partial\zeta} + \frac{\partial\delta z}{\partial\eta}\right]. \tag{27}$$

In the ultra-relativistic limit, $\beta_x^0 \to 1$ and $\gamma_0 \sim p_x^0/m_i c$. Therefore, as $m_i c\gamma_0 \simeq 2p_x^0$, one can rewrite equation (27) as

$$\frac{\partial}{\partial\varphi}\left[\frac{m_i c}{c}\frac{p_x^{0^3}}{m_i^3 c^3}\frac{\omega_0 m_i^2 c^2}{2p_x^{0^2}}\frac{\partial\delta x}{\partial\varphi}\right] = \frac{E_0^2}{2\pi\sigma_0\omega_0}\frac{1}{2}\,\left[\frac{\partial\delta y}{\partial\zeta} + \frac{\partial\delta z}{\partial\eta}\right],$$

$$\frac{\partial}{\partial\varphi}\left[\frac{p_x^0}{m_i c}\frac{\partial\delta x}{\partial\varphi}\right] = \frac{E_0^2}{2\pi\sigma_0\omega_0^2 m_i}\,\left[\frac{\partial\delta y}{\partial\zeta} + \frac{\partial\delta z}{\partial\eta}\right],$$

$$\boxed{\frac{\partial}{\partial\varphi}\left[\frac{p_x^0}{m_i c}\frac{\partial\delta x}{\partial\varphi}\right] = \frac{R(\varphi)}{2\pi}\,\left[\frac{\partial\delta y}{\partial\zeta} + \frac{\partial\delta z}{\partial\eta}\right].} \tag{28}$$

The above equation can also be written as

$$\frac{\partial^2\delta x}{\partial\varphi^2} + \frac{1}{p_x^0}\frac{\partial p_x^0}{\partial\varphi}\frac{\partial\delta x}{\partial\delta\varphi} = \frac{R(\varphi)}{2\pi}\frac{m_i c}{p_x^0}\left[\frac{\partial\delta y}{\partial\zeta} + \frac{\partial\delta z}{\partial\eta}\right]. \tag{28a}$$

Similarly, equation (10b) yields to

$$\frac{\mathrm{d}p_y}{\mathrm{d}\varphi} = \frac{E_0^2}{2\pi\sigma_0}\,\frac{m_i c\gamma_0 - p_x^0}{m_i c\gamma_0 + p_x^0}\left[\frac{\partial z}{\partial\zeta}\frac{\partial x}{\partial\eta} - \frac{\partial x}{\partial\zeta}\frac{\partial z}{\partial\eta}\right],$$

$$\frac{\partial}{\partial\varphi}\left[m_i\gamma_0\delta\dot{y}\right] = \frac{E_0^2}{2\pi\sigma_0\omega_0}\,\frac{m_i c\gamma_0}{m_i c\gamma_0 + p_x^0}\left[-\frac{\partial\delta x}{\partial\zeta}\left(1 + \frac{\partial\delta z}{\partial\eta}\right)\right],$$

$$\boxed{\frac{\partial}{\partial\varphi}\left[\frac{m_i c}{p_x^0}\frac{\partial\delta y}{\partial\varphi}\right] = -\frac{R(\varphi)}{2\pi}\frac{\partial\delta x}{\partial\zeta},} \tag{29}$$

where the product of perturbed terms is ignored.

For the z-component, one can obtain

$$\boxed{\frac{\partial}{\partial\varphi}\left[\frac{m_i c}{p_x^0}\frac{\partial\delta z}{\partial\varphi}\right]=-\frac{R(\varphi)}{2\pi}\frac{\partial\delta x}{\partial\eta}.} \tag{30}$$

Writing down all equations like equation (28a), one gets

$$\frac{\partial^2\delta x}{\partial\varphi^2}+\frac{1}{p_x^0}\frac{\partial p_x^0}{\partial\varphi}\frac{\partial\delta x}{\partial\delta\varphi}=\frac{R(\varphi)}{2\pi}\frac{m_i c}{p_x^0}\left[\frac{\partial\delta y}{\partial\zeta}+\frac{\partial\delta z}{\partial\eta}\right], \tag{28a}$$

$$\frac{\partial^2\delta y}{\partial\varphi^2}+\frac{1}{p_x^0}\frac{\partial p_x^0}{\partial\varphi}\frac{\partial\delta y}{\partial\delta\varphi}=-\frac{R(\varphi)}{2\pi}\frac{p_x^0}{m_i c}\frac{\partial\delta x}{\partial\zeta}, \tag{29a}$$

$$\frac{\partial^2\delta z}{\partial\varphi^2}+\frac{1}{p_x^0}\frac{\partial p_x^0}{\partial\varphi}\frac{\partial\delta z}{\partial\delta\varphi}=-\frac{R(\varphi)}{2\pi}\frac{p_x^0}{m_i c}\frac{\partial\delta x}{\partial\eta}. \tag{30a}$$

Supposing the perturbations have following shape

$$(\delta x,\delta y,\delta z)\sim(\delta\hat{x},\delta\hat{y},\delta\hat{z})\cdot\exp\left(\int_0^{\varphi}\Gamma(\varphi')\mathrm{d}\varphi'-iq\zeta-ir\eta\right), \tag{31}$$

where Γ is the growth rate and q and r are dimensionless parameters.

Then,

$$\left[\Gamma^2+\frac{\partial\Gamma}{\partial\varphi}+\frac{1}{p_x^0}\frac{\partial p_x^0}{\partial\varphi}\Gamma\right]\delta\hat{x}=\frac{R(\varphi)m_i c}{2\pi p_x^0}\cdot-i[q\delta\hat{y}+r\delta\hat{z}], \tag{32a}$$

$$\left[\Gamma^2+\frac{\partial\Gamma}{\partial\varphi}+\frac{1}{p_x^0}\frac{\partial p_x^0}{\partial\varphi}\Gamma\right]\delta\hat{y}=\frac{R(\varphi)p_x^0}{2\pi m_i c}\cdot iq\delta\hat{x}, \tag{32b}$$

$$\left[\Gamma^2+\frac{\partial\Gamma}{\partial\varphi}+\frac{1}{p_x^0}\frac{\partial p_x^0}{\partial\varphi}\Gamma\right]\delta\hat{z}=\frac{R(\varphi)p_x^0}{2\pi m_i c}\cdot ir\delta\hat{x}. \tag{32c}$$

In the ultra-relativistic limit, $p_x^0/m_i c\gg 1$ and the perturbations grow mainly in y- and z-direction. Thus, the growth rate is rather large and $\Gamma\gg 1$, $\Gamma^{-2}\,\partial_\varphi\Gamma\ll 1$.

Therefore, equations (32a), (32b) and (32c) result in

$$\Gamma^2 \delta\hat{x} = \frac{R(\varphi) m_i c}{2\pi p_x^0} \cdot -i[q\delta\hat{y} + r\delta\hat{z}], \tag{33a}$$

$$\Gamma^2 \delta\hat{y} = \frac{R(\varphi) p_x^0}{2\pi m_i c} \cdot iq\delta\hat{x}, \tag{33b}$$

$$\Gamma^2 \delta\hat{z} = \frac{R(\varphi) p_x^0}{2\pi m_i c} \cdot ir\delta\hat{x}. \tag{33c}$$

By multiplying equations (33b) and (33c) respectively by q and r and adding them together, one gets

$$\Gamma^2 (q\delta\hat{y} + r\delta\hat{z}) = \frac{R(\varphi) p_x^0}{2\pi m_i c} \cdot i(q^2 + r^2)\delta\hat{x}. \tag{34}$$

Furthermore, equation (33a) can be used to simplify equation (34) as

$$\Gamma^2 \Gamma^2 \left(\frac{2\pi}{R(\varphi)} \frac{p_x^0}{m_i c} \right) \frac{\delta\hat{x}}{-i} = \frac{R(\varphi)}{2\pi} \frac{p_x^0}{m_i c} \cdot i(q^2 + r^2)\delta\hat{x},$$

$$\Gamma^4 = \left(\frac{R(\varphi)}{2\pi} \right)^2 (q^2 + r^2). \tag{35}$$

This leads to the growth rate

$$\boxed{\Gamma = \left(\frac{R(\varphi)}{2\pi} \right)^{1/2} \left(q^2 + r^2 \right)^{1/4}.} \tag{36}$$

One can derive the asymptotic response of the perturbation by solving the equation for the phase by using equation (21). For doing so, one can simplify

$$\gamma_0 = \sqrt{1 + \frac{{p_x^0}^2}{m_i^2 c^2}},$$

$$\gamma_0 = \sqrt{1 + \left(\frac{W(\varphi)(W(\varphi)+2)}{2(W(\varphi)+1)}\right)^2},$$

$$\gamma_0 = \frac{W(\varphi)^2 + 2W(\varphi) + 2}{2(W(\varphi)+1)}. \tag{37}$$

Integrating equation (17), one can get

$$\int_0^\varphi \mathrm{d}\varphi' \left(1 - \frac{p_x^0}{m_i c \gamma_0}\right)^{-1} = \int_0^t \mathrm{d}t'\, \omega_0,$$

$$\int_0^\varphi \mathrm{d}\varphi' \left(1 - \frac{W(W+2)}{2(W+1)} \cdot \frac{2(W+1)}{W^2+2W+2}\right)^{-1} = \omega_0\, t,$$

$$\int_0^\varphi \mathrm{d}\varphi' \left(1 - \frac{W(W+2)}{W^2+2W+2}\right)^{-1} = \omega_0\, t,$$

$$\int_0^\varphi \mathrm{d}\varphi' \frac{1}{2}\left(W^2+2W+2\right) = \omega_0\, t,$$

$$\boxed{\varphi + \int_0^\varphi \mathrm{d}\varphi' \left(\frac{1}{2}W^2 + W\right) = \omega_0\, t,} \tag{38}$$

where $W(\varphi') = W$.

Analog for the space coordinate, as

$$\frac{\mathrm{d}\varphi}{\mathrm{d}x} = \omega_0 \left(\frac{\mathrm{d}t}{\mathrm{d}x} - \frac{1}{c}\right) \implies \frac{\mathrm{d}t}{\mathrm{d}x} = \frac{1}{\omega_0}\frac{\mathrm{d}\varphi}{\mathrm{d}x} + \frac{1}{c},$$

$$\frac{\mathrm{d}x}{\mathrm{d}\varphi} = \frac{\mathrm{d}x}{\mathrm{d}t} \cdot \frac{\mathrm{d}t}{\mathrm{d}\varphi} = \frac{1}{\omega_0}\left[1 + W + \frac{W^2}{2}\right]\left[\frac{1}{\omega_0}\frac{\mathrm{d}\varphi}{\mathrm{d}x} + \frac{1}{c}\right]^{-1},$$

$$\frac{1}{\omega_0}\frac{\mathrm{d}x}{\mathrm{d}\varphi}\frac{\mathrm{d}\varphi}{\mathrm{d}x}+\frac{1}{c}\frac{\mathrm{d}x}{\mathrm{d}\varphi}=\frac{1}{\omega_0}\left[1+W+\frac{W^2}{2}\right],$$

$$\frac{\mathrm{d}x}{\mathrm{d}\varphi}=\frac{c}{\omega_0}\left[W\left(1+\frac{W}{2}\right)\right],$$

$$\frac{\mathrm{d}\varphi}{\mathrm{d}x}=\frac{\omega_0}{c}\left[W\left(1+\frac{W}{2}\right)\right]^{-1}, \tag{39}$$

following equation can be obtained by integrating equation (39):

$$\int_0^{\varphi}\mathrm{d}\varphi'\,W\left(1+\frac{W}{2}\right)=\int_0^{x}\mathrm{d}x'\,\frac{\omega_0}{c},$$

$$\boxed{\int_0^{\varphi}\mathrm{d}\varphi'\left(\frac{1}{2}W^2+W\right)=\frac{\omega_0}{c}\,x.} \tag{40}$$

For a constant laser pulse amplitude, when $R = R_0$, one can get $W(\varphi) = (R_0/\lambda_0)\,\varphi$. Therefore, euqations (38) and (40) yield respectively to

$$\boxed{\begin{aligned}\varphi+\left(\frac{R_0}{\lambda_0}\right)\frac{\varphi^2}{2}+\left(\frac{R_0}{\lambda_0}\right)^2\frac{\varphi^3}{6}&=\omega_0\,t, &\text{(41a)}\\ \left(\frac{R_0}{\lambda_0}\right)\frac{\varphi^2}{2}+\left(\frac{R_0}{\lambda_0}\right)^2\frac{\varphi^3}{6}&=\frac{\omega_0}{c}\,x. &\text{(41b)}\end{aligned}}$$

From equation (41a), the asymptotic early- and late-time evolution of ions momenta can be obtained. For the early-time asymptotic, $t \ll \lambda_0/\omega_0 R_0$ or rather $\omega_0 t R_0/\lambda_0 \ll 1$ and therefore the first term of equation (41a) dominates giving $t \approx \omega_0 t$.

Then, for $R_0/\lambda_0 \ll 1$, the momentum is

$$p_x = m_i c \left(\frac{R_0}{\lambda_0}\right) \varphi \frac{\left[\left(\frac{R_0}{\lambda_0}\right)\varphi + 2\right]}{2\left[\left(\frac{R_0}{\lambda_0}\right)\varphi + 1\right]},$$

$$p_x \simeq m_i c \left(\frac{R_0}{\lambda_0}\right) \varphi,$$

$$\boxed{p_x \simeq m_i c \left(\frac{R_0}{\lambda_0}\right) \omega_0 \, t.} \tag{42}$$

For the late-time asymptotic, $t \gg 1/\omega_0(\lambda_0/R_0)$ or rather $(R_0/\lambda_0)\omega_0 t \gg 1$, the last term of equation (41a) dominates and therefore $\varphi^3 \approx 6\,\omega_0 t(\lambda_0/R_0)^2$. Then, the expression of the momentum is

$$p_x \simeq m_i c \left(\frac{R_0}{\lambda_0}\right) \varphi,$$

$$p_x \simeq m_i c \left(\frac{R_0}{\lambda_0}\right) \left[6\,\omega_0 t \left(\frac{\lambda_0}{R_0}\right)^2\right]^{1/3},$$

$$\boxed{p_x \simeq m_i c \left(\frac{3}{4}\frac{R_0}{\lambda_0}\,\omega_0 t\right)^{1/3}.} \tag{43}$$

Analog, one can obtain relationships between the phase φ and x using equation (41b). Therefore, the transverse perturbation growth is

$$\delta y \sim \exp\left(\int_0^{\varphi} \Gamma(\varphi')\mathrm{d}\varphi' - iq\zeta - ir\eta\right). \tag{44}$$

For a constant laser pulse, equation (44) leads to

$$\delta y \sim \exp\left(\Gamma(\varphi)\varphi - iq\zeta - ir\eta\right). \tag{45}$$

Using equations (36) and (43) leads to the perturbation growth rate

$$\Gamma = \left(\frac{R(\varphi)}{2\pi}\right)^{1/2} \left(q^2 + r^2\right)^{1/4}. \tag{46}$$

The long-term asymptote for the transversal perturbation is then

where

$$\boxed{\delta y \sim \exp\left[\left(\frac{t}{\tau_r}\right)^{1/3} - iq\zeta - ir\eta\right],} \tag{47}$$

$$\boxed{\tau_r = \frac{(2\pi)^3}{6\omega_0} \frac{R_0^{1/2}}{\lambda_0^2} \frac{1}{\left(q^2 + r^2\right)^{3/4}}} \tag{48}$$

is the time constant of the exponential decay.

The early-time asymptote can describe the non-relativistic growth of the perturbation which grows like $\delta y \sim \exp(t/\tau_r - iq\zeta - ir\eta)$ with $\tau_r = 2\pi \left[\omega_0 R_0^{1/2} \left(q^2 + r^2\right)^{1/4}\right]^{-1}$. Therefore, as one has t instead of $t^{1/3}$, the instability increases with time faster than in the ultra-relativistic regime. We will focus on the ultra-relativistic case, as we are only interested in the high energetic case or rather the regime where we have the better growth reduction of the the instabilities.

2.2.3 Interchange instability: Solving the equilibrium of motion for a modulated target

We will now investigate the instabilities for a surface modulated target in transverse directions. For this case, the initial conditions are

$$x = 0, \qquad y = \zeta + a_m \exp(ik_m\zeta), \qquad z = \eta + a_m \exp(ik_m\eta).$$

Like before, one can solve the equilibrium solution of momentum for the x-component

$$\frac{\mathrm{d}p_x^0}{\mathrm{d}t} = \frac{E_0^2}{2\pi\sigma_0}\frac{m_i c\gamma_0 - p_x^0}{m_i c\gamma_0 + p_x^0}\left[\frac{\partial y}{\partial\zeta}\frac{\partial z}{\partial\eta} - \frac{\partial z}{\partial\zeta}\frac{\partial y}{\partial\eta}\right],$$

$$\frac{\mathrm{d}p_x^0}{\mathrm{d}t} = \frac{E_0^2}{2\pi\sigma_0}\frac{m_i c\gamma_0 - p_x^0}{m_i c\gamma_0 + p_x^0}\left(1 + ik_m l_y\right)\left(1 + ik_m l_z\right), \tag{49}$$

where $l_y = a_m \exp(ik_m\zeta)$ and $l_z = a_m \exp(ik_m\eta)$.

The momentum is therefore

$$p_x^0 = m_i c\frac{W(W+2)}{2(W+1)}, \tag{50}$$

where $W = W(\varphi)$ contains additional factors

$$W(\varphi) = \int_0^{\varphi}\frac{E_0^2(\varphi)}{m_i\omega_0^2\sigma_0\lambda_0}\left(1 + ik_m l_y\right)\left(1 + ik_m l_z\right). \tag{51}$$

Like equations (27) to (30), one proceeds similarly in order to get the three equations for investigating the instability. Therefore, one has

$$\frac{\mathrm{d}}{\mathrm{d}\varphi}\left[p_x^0 + m_i c\gamma_0^3\frac{\delta\dot{x}}{c}\right] = \frac{E_0^2 m_i c\gamma_0}{2\pi\sigma_0\omega_0(m_i c\gamma_0 + p_x^0)}\left[\left(\frac{\partial\delta y}{\partial\zeta} + 1 + ik_m l_y\right)\right.$$
$$\left.\cdot\left(\frac{\partial\delta z}{\partial\eta} + 1 + ik_m l_z\right)\right],$$

$$\frac{\mathrm{d}}{\mathrm{d}\varphi}\left[p_x^0 + m_i c\gamma_0^3\frac{\delta\dot{x}}{c}\right] = \frac{E_0^2 m_i c\gamma_0}{2\pi\sigma_0\omega_0(m_i c\gamma_0 + p_x^0)}\left[\frac{\partial\delta y}{\partial\zeta}\left(1 + ik_m l_z\right)\right.$$
$$\left. + \left(1 + ik_m l_y\right)\left(1 + ik_m l_z\right) + \frac{\partial\delta z}{\partial\eta}\left(1 + ik_m l_y\right) + \frac{\partial\delta y}{\partial\zeta}\frac{\partial\delta z}{\partial\eta}\right]. \tag{52}$$

As

$$\frac{\mathrm{d}p_x^0}{\mathrm{d}\varphi} = \frac{E_0^2}{2\pi\sigma_0\omega_0}\frac{m_i c\gamma_0}{m_i c\gamma_0 + p_x^0}\left(1 + ik_m l_y\right)\left(1 + ik_m l_z\right), \tag{53}$$

then

$$\frac{\mathrm{d}}{\mathrm{d}\varphi}\left[m_i c\gamma_0^3\frac{\delta\dot{x}}{c}\right]=\frac{E_0^2 m_i c\gamma_0}{2\pi\sigma_0\omega_0(m_i c\gamma_0+p_x^0)}\left[\frac{\partial\delta y}{\partial\zeta}\left(1+ik_m l_z\right)+\frac{\partial\delta z}{\partial\eta}\left(1+ik_m l_y\right)\right], \quad (54)$$

where $\partial_\zeta\delta y\cdot\partial_\eta\delta z$ are ignored due to perturbed quantities. After simplifications, this results in

$$\frac{\partial}{\partial\varphi}\left[\frac{p_x^0}{m_i c}\frac{\partial\delta x}{\partial\varphi}\right]=\frac{R(\varphi)}{2\pi}\left[\frac{\partial\delta y}{\partial\zeta}\left(1+ik_m l_z\right)+\frac{\partial\delta z}{\partial\eta}\left(1+ik_m l_y\right)\right], \quad (55a)$$

$$\frac{\partial}{\partial\varphi}\left[\frac{m_i c}{p_x^0}\frac{\partial\delta y}{\partial\varphi}\right]=-\frac{R(\varphi)}{2\pi}\left[\frac{\partial\delta x}{\partial\zeta}\left(1+ik_m l_z\right)\right], \quad (55b)$$

$$\frac{\partial}{\partial\varphi}\left[\frac{m_i c}{p_x^0}\frac{\partial\delta z}{\partial\varphi}\right]=-\frac{R(\varphi)}{2\pi}\left[\frac{\partial\delta x}{\partial\eta}\left(1+ik_m l_y\right)\right], \quad (55c)$$

where equations (55b) and (55c) are analogically obtained and $R(\varphi)$ remains the same like in equation (20).

Supposing

$$\delta x,\delta y,\delta z\sim(\delta\hat{x},\delta\hat{y},\delta\hat{z})\exp\left(\int_0^\varphi\Gamma(\varphi')\mathrm{d}\varphi'-iq\zeta-ir\eta\right). \quad (56)$$

Then, one can get

$$\left[\Gamma^2+\frac{\partial\Gamma}{\partial\varphi}+\frac{1}{p_x^0}\frac{\partial p_x^0}{\partial\varphi}\Gamma\right]\delta\hat{x}=\frac{R(\varphi)m_i c}{2\pi p_x^0}\cdot-i\left[q(1+ik_m l_z)\delta\hat{y}+r(1+ik_m l_y)\delta\hat{z}\right], \quad (57a)$$

$$\left[\Gamma^2+\frac{\partial\Gamma}{\partial\varphi}+\frac{1}{p_x^0}\frac{\partial p_x^0}{\partial\varphi}\Gamma\right]\delta\hat{y}=\frac{R(\varphi)p_x^0}{2\pi m_i c}\cdot iq(1+ik_m l_z)\delta\hat{x}, \quad (57b)$$

$$\left[\Gamma^2+\frac{\partial\Gamma}{\partial\varphi}+\frac{1}{p_x^0}\frac{\partial p_x^0}{\partial\varphi}\Gamma\right]\delta\hat{z}=\frac{R(\varphi)p_x^0}{2\pi m_i c}\cdot ir(1+ik_m l_y)\delta\hat{x}. \quad (57c)$$

As before, since $\Gamma \gg 1$, $\Gamma^{-2}\,\partial_\varphi \Gamma \ll 1$, equations (57a), (57b) and (57c) yield

$$\Gamma^2 \delta\hat{x} = \frac{R(\varphi) m_i c}{2\pi p_x^0} \cdot -i \left[q(1 + ik_m l_z)\delta\hat{y} + r(1 + ik_m l_y)\delta\hat{z} \right], \tag{58a}$$

$$\Gamma^2 \delta\hat{y} = \frac{R(\varphi) p_x^0}{2\pi m_i c} \cdot iq(1 + ik_m l_z)\delta\hat{x}, \tag{58b}$$

$$\Gamma^2 \delta\hat{z} = \frac{R(\varphi) p_x^0}{2\pi m_i c} \cdot ir(1 + ik_m l_y)\delta\hat{x}, \tag{58c}$$

By multiplying equations (58b) and (58c) respectively by $q(1 + ik_m l_z)$ and $r(1 + ik_m l_y)$ and adding them together, the result is

$$\Gamma^2 \left[q(1 + ik_m l_z)\delta\hat{y} + r(1 + ik_m l_y)\delta\hat{z} \right] = \frac{R(\varphi) p_x^0}{2\pi m_i c} \cdot i \left[q^2(1 + ik_m l_z)^2 + r^2(1 + ik_m l_y)^2 \right] \delta\hat{x} \tag{59}$$

Furthermore, equation (58a) can be used to simplify equation (59) as

$$\Gamma^2 \delta\hat{x} = \frac{-i}{\Gamma^2} \frac{R(\varphi) p_x^0}{2\pi m_i c} \frac{R(\varphi) m_i c}{2\pi p_x^0} \cdot i \left[q^2(1 + ik_m l_z)^2 + r^2(1 + ik_m l_y)^2 \right] \delta\hat{x},$$

$$\Gamma^4 = \left(\frac{R(\varphi)}{2\pi} \right)^2 \cdot i \left[q^2(1 + ik_m l_z)^2 + r^2(1 + ik_m l_y)^2 \right]. \tag{60}$$

If $l_y = l_z = l_m$, then

$$\Gamma^4 = \left(\frac{R(\varphi)}{2\pi} \right)^2 \cdot i \left(1 + ik_m l_m\right) \left(q^2 + r^2\right),$$

$$\boxed{\Gamma = \left(\frac{R(\varphi)}{2\pi} \right)^{1/2} \cdot i \left(1 + ik_m l_m\right)^{1/2} \left(q^2 + r^2\right)^{1/4}.} \tag{61}$$

As before, one can determine the long-term asymptote from equation (41a). However, in this case, R_0 contains the additional factor $(1 + ik_m l_m)^2$. Hence, one can

rewrite equation (41a) as

$$\varphi + \left(\frac{R_0}{\lambda_0}\right)\frac{\varphi^2}{2}\left(1 + ik_m l_m\right)^4 + \left(\frac{R_0}{\lambda_0}\right)^2\frac{\varphi^3}{6}\left(1 + ik_m l_m\right)^4 = \omega_0\, t. \tag{62}$$

For the late-time asymptote, this leads to

$$\varphi^3 \simeq 6\omega_0 t\left(\frac{\lambda_0}{R_0}\right)^2\left[1 + ik_m l_m\right]^{-4}. \tag{63}$$

Then, the transversal perturbation growth rate is written as

$$\delta y \sim \exp\left[\Gamma(\varphi)\varphi - iq\zeta - ir\eta\right],$$

where

$$\boxed{\delta y \sim \exp\left[\left(\frac{t}{\tau_r}\right)^{1/3} - iq\zeta - ir\eta\right],} \tag{64}$$

$$\boxed{\tau_r = \frac{(2\pi)^3}{6\omega_0}\frac{R_0^{1/2}}{\lambda_0^2}\frac{\left(1 + ik_m l_m\right)^{5/6}}{\left(q^2 + r^2\right)^{3/4}}.} \tag{65}$$

For $|k_m l_m| \gg 1$, τ_r is increased and therefore a reduction in the growth rate is possible if

$$k_m l_m > \left(\sqrt{\frac{3}{8}} - \frac{1}{\sqrt{2}}\right), \tag{66}$$

where the $(5/6)^{\text{th}}$ root of i were taking for the inequality. Hence, equation (65) can be rewritten as

$$\boxed{\tau_r = \frac{(2\pi)^3}{6\omega_0}\frac{R_0^{1/2}}{\lambda_0^2}\frac{\left(k_m l_m\right)^{5/6}}{\left(q^2 + r^2\right)^{3/4}}\left(\sqrt{\frac{3}{8}} - \frac{1}{\sqrt{2}}\right).} \tag{67}$$

3 Numerical analysis of the RTI

3.1 Defining the profile of the system before PIC-simulation

As theory is explained so far, we want to do particle-in-cell (PIC) simulations in order to investigate the behaviour of the system considering the parameters obtained in theory. That is why we have to implement the different parameters into the namelist. SMILEI (version 4.2) will be used for the PIC-simulations.

3.1.1 Parameters of the simulation

We will use a simulation box of the size of $L_x \times L_y = 18\lambda_0(x) \times 10\lambda_0(y)$ where $\lambda_0 = 0.8 \times 10^{-6}\,\mathrm{m}$ is the laser wavelength (which correspond to $1800(x) \times 1000(y)$ cells with a cell length of $0.06\lambda_0$). The time step of the simulation is $4.19\,\tau_L \cdot 10^{-2}$ where $\tau_L = 2\pi/\omega_0 = 2.67$ fs is the laser period. A total of 1.5×10^4 iterations will be made. We use 16 particles per cell with only a foil target consisting of electrons and ions.

As we want to exclude other effects occurring due to the laser shape, we will consider only plane waves in the simulations. In addition, we will focus on a laser with a constant temporal intensity profile. This ideal laser can be approximated to a real laser considering that the laser wavelength is much smaller than the whole target front.

3.1.2 Shape and density parameters of the target

As mentioned in section 2.1.3, we will have several target shapes with different modulations. In all cases, the modulation is on the left side, where the laser pulse incident on the target. The following shapes were used:

- ***Surface modulated target with rectangular grooves with changing ion density (rec)***

  The $1\lambda_0$ thick target is located in the region $1\lambda_0 \leq x \leq 2\lambda_0$ and has a rectangular modulation initially located in the region $1\lambda_0 - a_m \leq x \leq 1\lambda_0 + a_m$, where a_m is the amplitude of the modulation and λ_0 the laser wavelength.

  The density modulated surface profile looks like[1]:

$$\boxed{n(x, y) = \text{trap}(x, z) \cdot (a_m \cos(k_m y) - a_m)} \tag{68}$$

  where $\text{trap}(x, z)$ is a trapezoidal function, a_m the amplitude and k_m the wave vector of the modulation.

- ***Rippled target with constant plasma density (rp)***

  The $1\lambda_0$ thick target is located in the region $1\lambda_0 \leq x \leq 2\lambda_0$ and has a rippled modulation initially located in the region $1\lambda_0 - a_m \cdot \cos(k_m y) \leq x \leq 1\lambda_0 + a_m$.

  The density modulated surface profile looks like[1]:

$$\boxed{n(x, y) = n_0} \tag{69}$$

  where $n_0 = 250\, n_c$ is the constant density.

- ***Rippled target with changing plasma density (rpg)***

  The $1\lambda_0$ thick target is located in the region $1\lambda_0 \leq x \leq 2\lambda_0$ and has a rippled modulation initially located in the region $1\lambda_0 + a_m \cdot \cos(k_m y) \leq x \leq 1\lambda_0 + a_m$, where a_m is the amplitude of the modulation and λ_0 the laser wavelength.

[1] the code for the density profile is in appendix

The density modulated surface profile looks like[1]:

$$n(x, y) = \text{trap}(x, z) \cdot (a_m \cos(k_m y) - a_m) \tag{70}$$

- ***1λ_0 density modulated target with changing plasma density (1λ_0 dm)***

  The $1\lambda_0$ thick target is located in the region $1\lambda_0 \leq x \leq 2\lambda_0$ and is integrally modulated with lowest density value of $n_{min} = 0.5\, n_{max}$.

  The density modulated surface profile looks like[1]:

$$n(x, y) = \text{trap}(x, z) \cdot \left(\frac{1}{2}\, a_m \left[3 + \cos(k_m y) \right] \right) \tag{71}$$

- ***2λ_0 density modulated target with changing plasma density (2λ_0 dm)***

  This target is exactly the same like above except that the target is $2\lambda_0$-thick and therefore located in the region $1\lambda_0 \leq x \leq 3\lambda_0$.

3.2 Results of the PIC-simulations

3.2.1 Density profile

Before checking the energy spectrum, one has to check the self made density profiles. For doing so, the ion density is plotted for $t = 0$. These are the modulation density profiles from simulation:

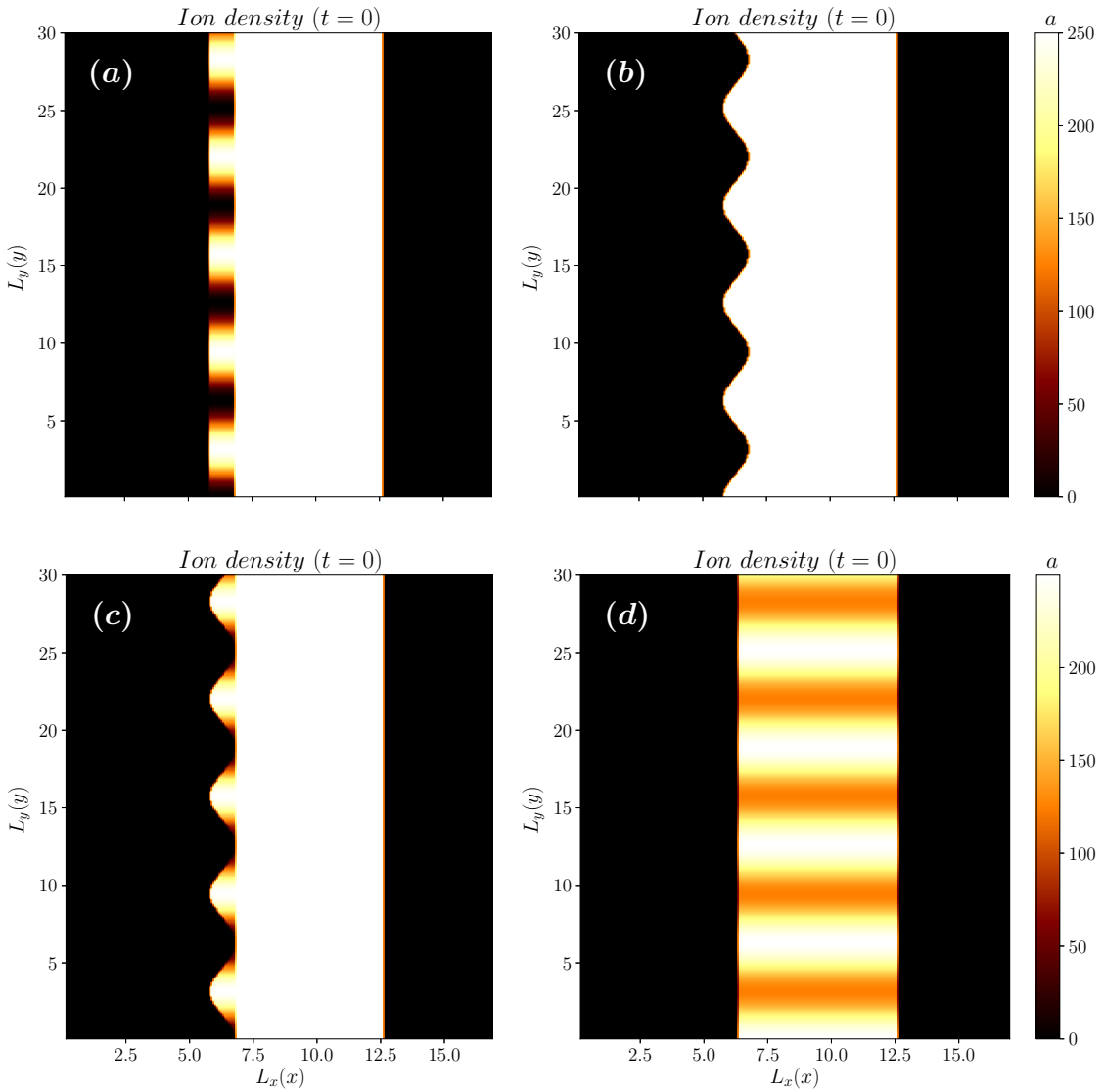

Figure 1: the different modulation density profiles of the target (zoomed in, for $k_m = 1$ and $a_m = 0.5$: **(*a*)** the rectangular groove modulated target with changing density at the front (rec), **(*b*)** the rippled modulated target (rp), **(*c*)** the rippled modulated target with changing density at the front (rpg) and **(*d*)** the $1\lambda_0$ density modulated target (1λ dm). The last shape (2λ dm) is similar to **(*d*)**, $a = n_0/n_c$ and L_x and L_y are in units of $\lambda_0/2\pi$.

As all target shapes are checked, one can analyze the instabilities by plotting at first the Energy spectrum of the ions.

3.2.2 Energy profile

For analyzing the instability growth and compare it to theory, the energy spectrum with the thinnest *i.e* sharpest dominant peak will be plotted. For doing so, one can define ΔE as the energy difference *i.e* the full width at half maximum (FWHM) of the dominant peak and E_{max} the peak maximum. As long as we have no idea where the sharpest peaks are, one can plot for (with a iteration step of 30 $\times$ time step) k_m, a_m and all shapes $\Delta E/E_{max}$ against time *i.e* against t/τ_L where τ_L is the laser period.

A self made python program[2] will iterate over each timestep and calculate $\Delta E/E_{max}$ for each time. The result of one of the plots are in figure 2. Noticed, that the single points around $1400 < t/\tau_L < 2000$ are values of the FWHM (full-width-at-half-maximum) which are not properly captured from the python-program as the roots for the FWHM mismatched when too many peaks are displayed. However, this will pose only a problem for the data from the density modulated target with low a_m. Actually, in this case, one can rather plot an animation of the ion spectra and look manually in time for the sharpest peak. This method allows an analysis for a_m down to 0.1 for density modulated targets and $a_m = 0.01$ for surface-modulated targets.

In all plots (*i.e* like figure 2), one can see that the value of the peak maximum shifts more and more to higher energies until a breakpoint (in figure 2c, which one can estimate the breakpoint at around $t/\tau_L \approx 1025$). With these information, the region around the breakpoint can now be iterated with a step of 1 $\times$ time step, and the energy spectrum of the sharpest peak can be plotted (see figure 4). This procedure will be done for all a_m, k_m and all target shapes (globally 80 times). The non-modulated target will be the reference and is shown in figure 3a and figure 3b

[2] the code is in appendix

with respectively the widths of $1\lambda_0$ and $2\lambda_0$, where only the first zoom is displayed.

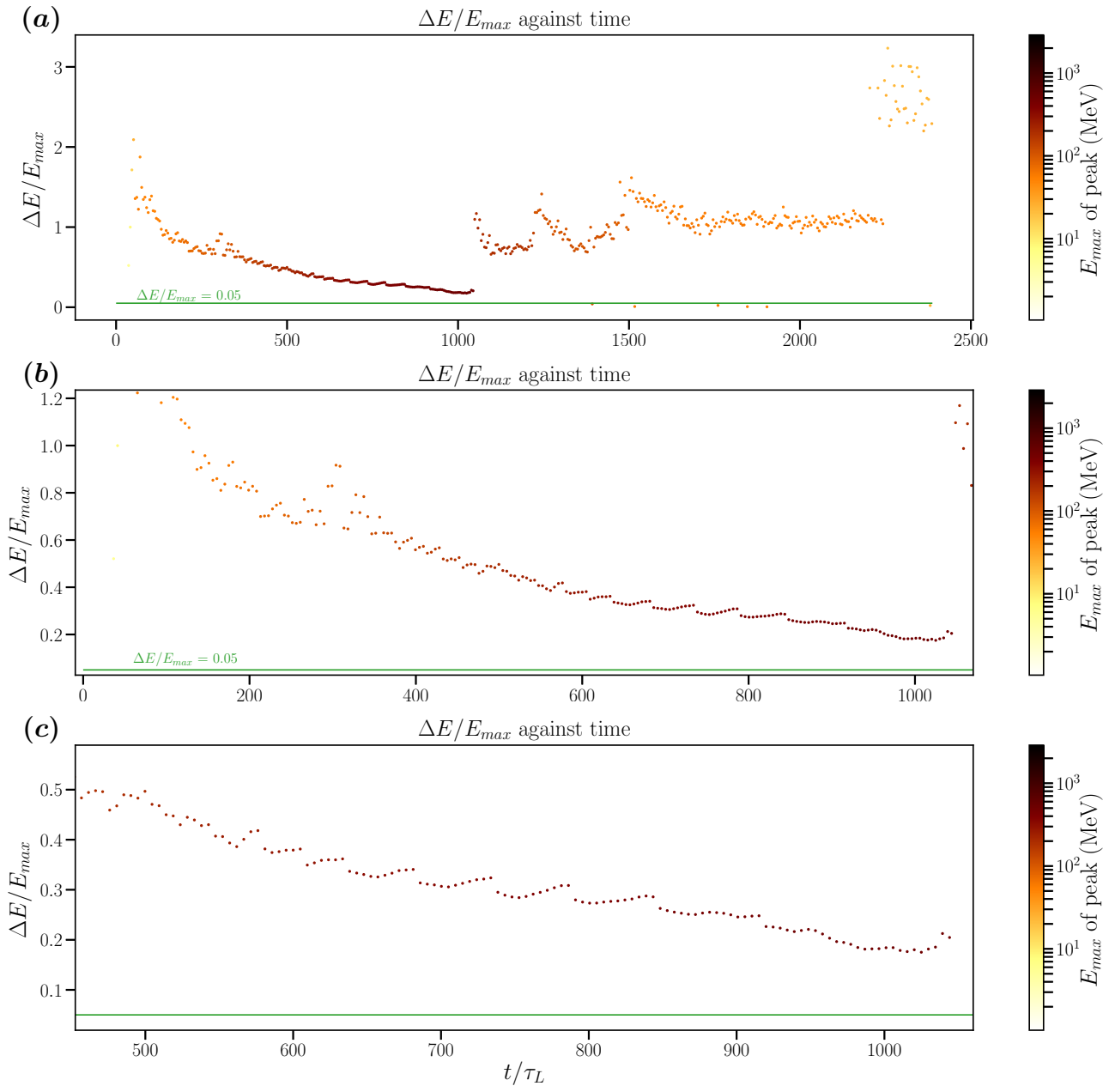

Figure 2: $\Delta E/E_{max}$ over t/τ_L where τ_L is the laser period with the rec modulated target at $k_m = 1$ and $a_m = 0.5$. **(a)** the density simulation time plotted, **(b)** zoom in the linear area, **(c)** zoom in the lowest area. Here is the green line the limit of $\Delta E/E_{max} = 0.05$ which is seeked and the color of the scatter is the value of the peak maximum.

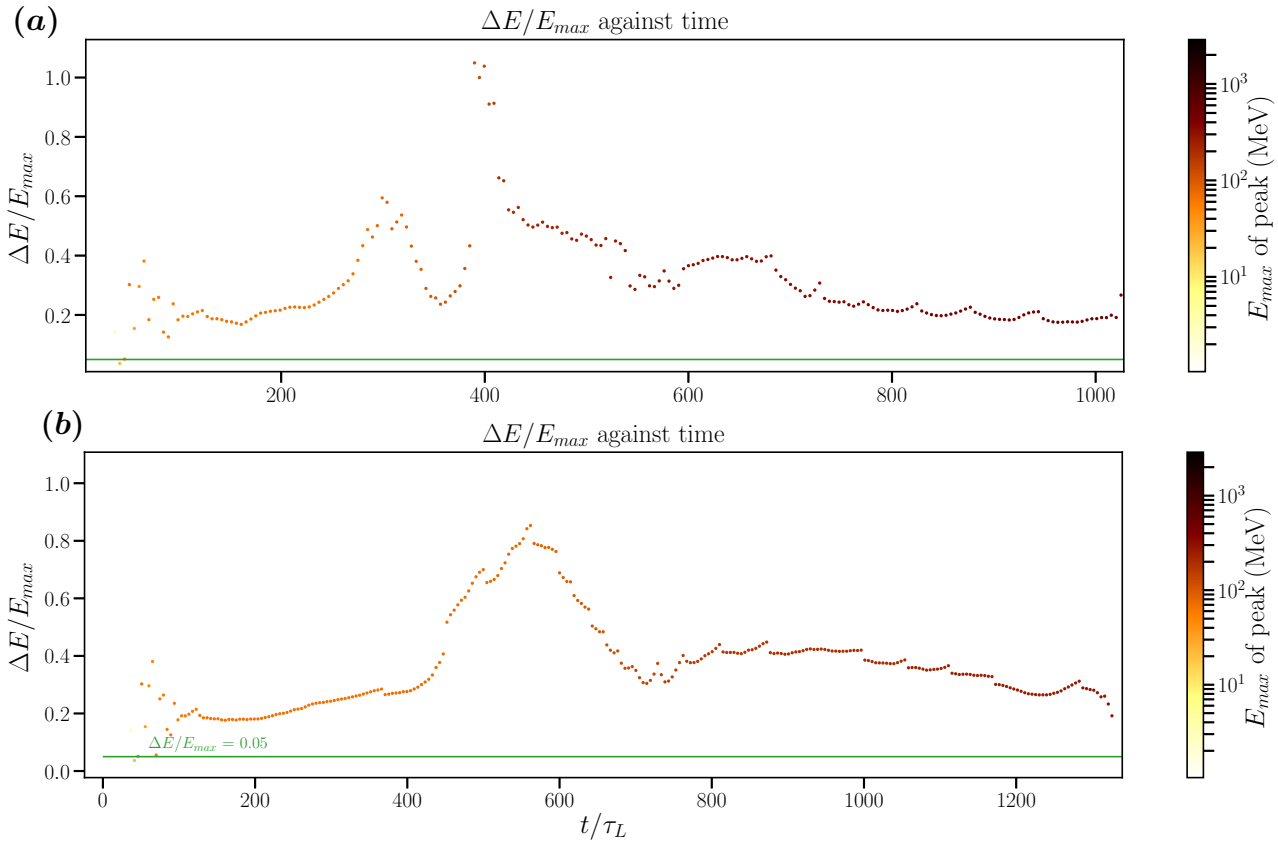

Figure 3: $\Delta E/E_{max}$ over t/τ_L where τ_L is the laser period with the non-modulated target zoomed *i.e* best simulation time plotted for **(*a*)** $1\lambda_0$ width and **(*b*)** $2\lambda_0$ width. Here is the green line the limit of $\Delta E/E_{max} = 0.05$ which is sought and the color of the scatter is the value of the peak maximum.

One can see between figure 2c and 3a , that the FWHM of the peak for the rectangular groove modulated target has a barely lower value of $\Delta E/E_{max}$ than the $1\lambda_0$ width non-modulated target (this will be more evident in figure 4). This is the first evidence, that surface-modulated targets can suppress instabilities.

In addition, figure 3 refers the difference between the two widths: for high energies, the $1\lambda_0$ width non-modulated target has a higher value of E_{max} at the end and a lower value of $\Delta E/E_{max}$, *i.e* a sharper peak and slightly higher peak maximum in the energy spectrum than the one with a $2\lambda_0$ width. This can be explained by the fact that the heated electrons in the front surface *i.e* in the skin-depth layer reached

almost the back of the target as $ds \sim c\sqrt{\gamma_0}/\omega_p \approx 1\,\mu\text{m} = \lambda_0$ (with ds the skin-deph layer thickness). With a thinner target width, the RPA of ions takes less time to start operating and thus, higher energies can be reached. In general, for a good RPA of ions, one should get $ds < \ell_0 < \lambda_0$[3].

After knowing where the sharpest peaks with the highest values of E_{max} are displayed, one can plot the ion energy spectrum of the time step, automatically given from the self made python program. This allows a better viewing into the energy spectrum of each single case especially the weight $i.e$ $\mathrm{d}N/\mathrm{d}\varepsilon$, the particle per energy.

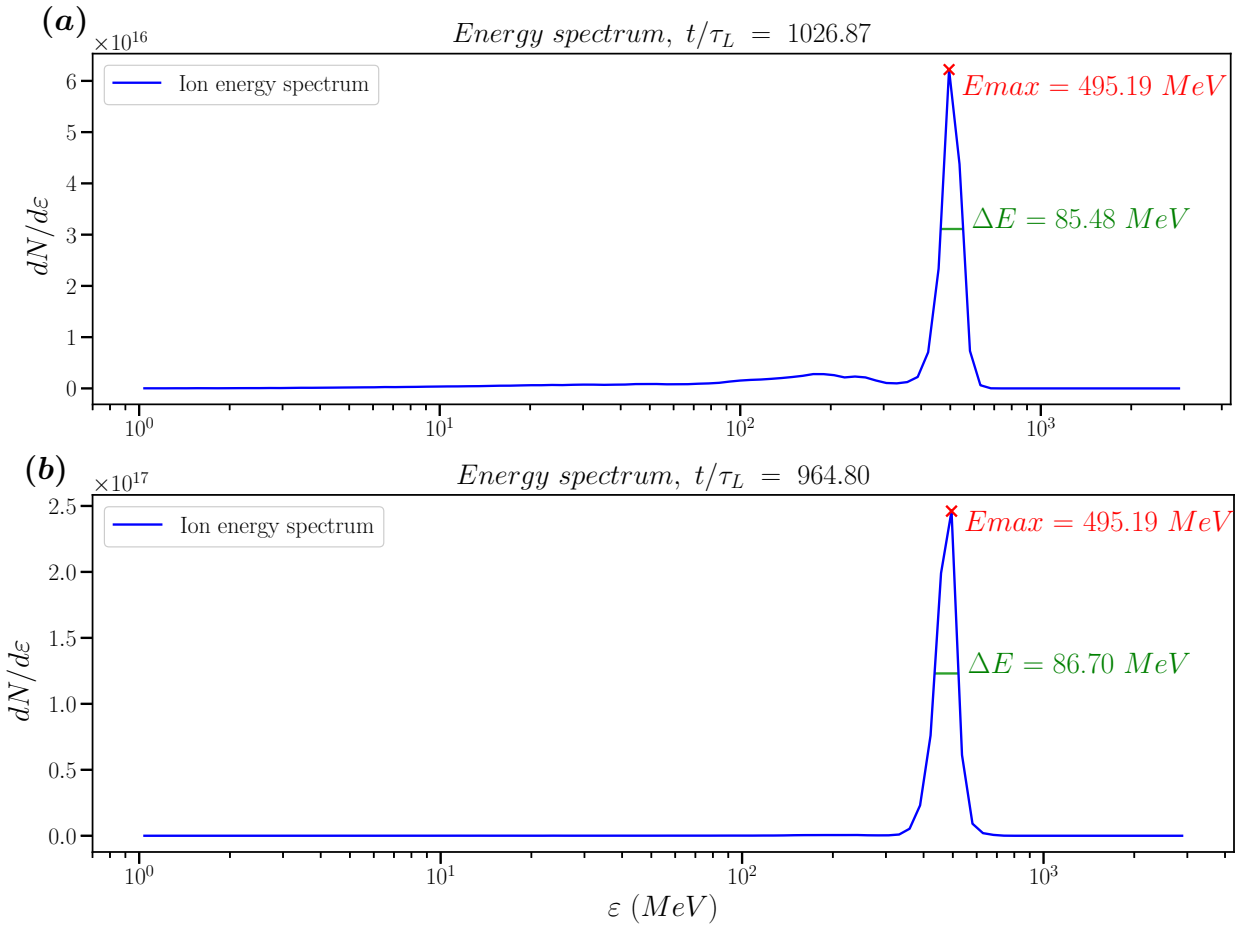

Figure 4: Energy spectrum of **(*a*)** the rec surface-modulated target and **(*b*)** the non-modulated target (both for $1\lambda_0$ width).

[3] If $ds > \ell_0$, we are in the BOA regime, which is less effective than RPA

One can see, that only the FWHM and the particle number per energy differ between figures 4a and 4b: After modulation, fewer ions are accelerated for the same maximum energy peak. This can be explained with the loss of plasma which goes into the vacuum as the time step is also quite advanced. The FWHM of the peak is only little varying due to the loss.

In order to compare the peaks of each a_m and k_m, we plot a_m against k_m with E_{max} in third dimension. As data points are generated, one can interpolate the values of E_{max} and generate then a map. This will allow us to look at all best data points at one time. At first, a linear interpolation is made, followed by a cubic interpolation. We suppose therefore, that the behaviour of E_{max} matches better with the cubic interpolation. We do the same for $\Delta E/E_{max}$.

Results for E_{max} and $\Delta E/E_{max}$ for the density modulated target are shown in figure 5 and figure 6.

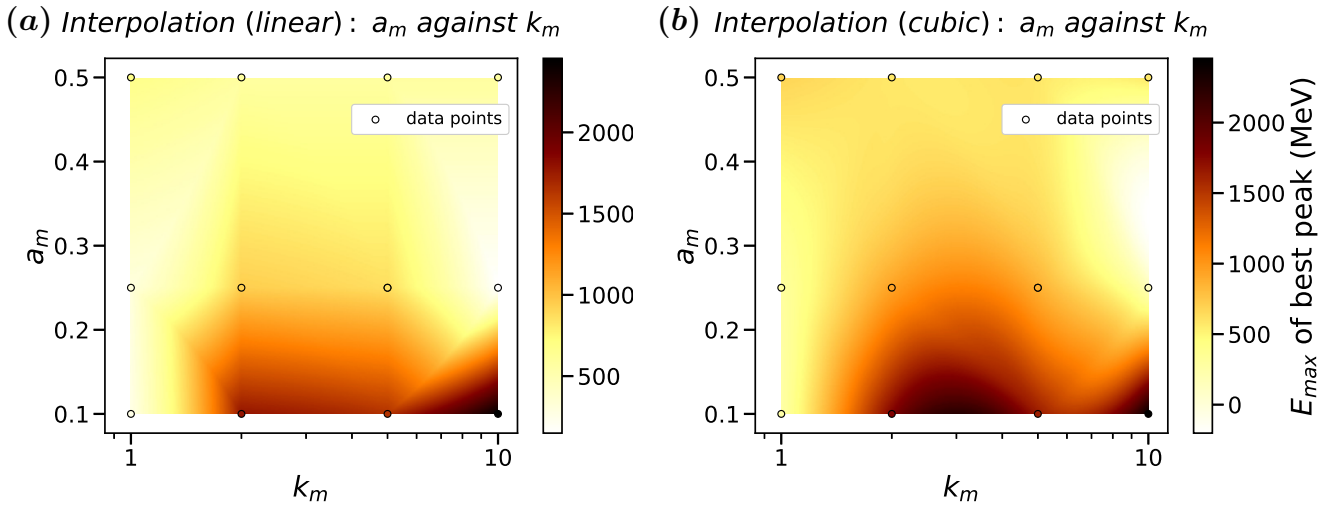

Figure 5: linear $(\boldsymbol{a})$ and cubic $(\boldsymbol{b})$ interpolation of the data for the $1\lambda_0$ density modulated target shape: related a_m and k_m with E_{max} in third dimension.

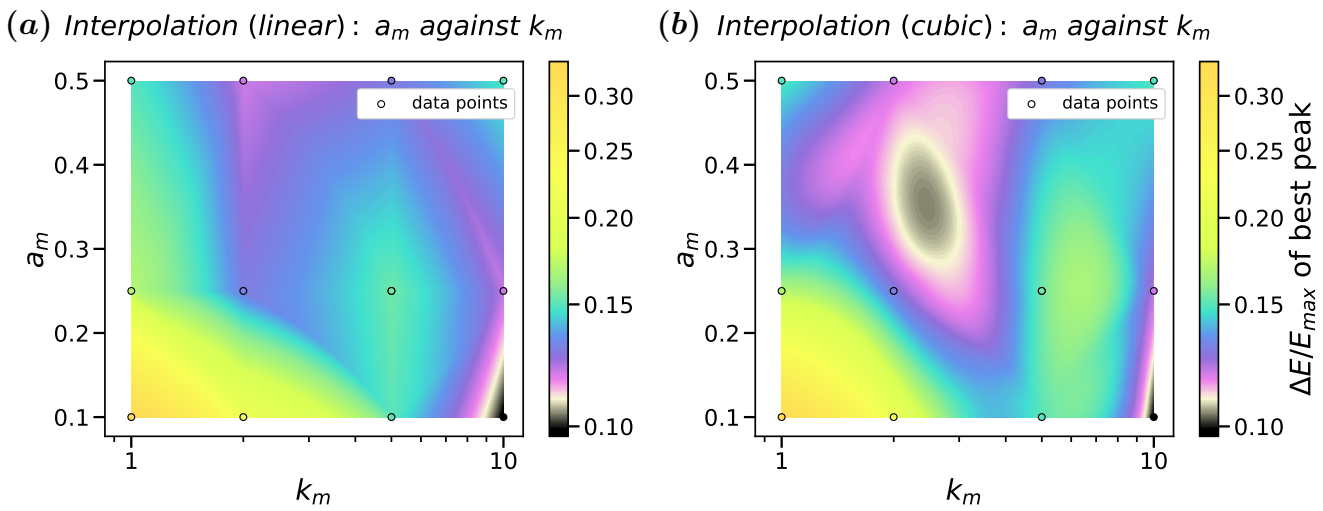

Figure 6: linear $(\boldsymbol{a})$ and cubic $(\boldsymbol{b})$ interpolation of the data for the $1\lambda_0$ density modulated target shape: related a_m and k_m with $\Delta E/E_{max}$ in third dimension.

In order to compare the regions where E_{max} is maximized and $\Delta E/E_{max}$ is minimized, one needs to only plot the cubic interpolation and display them both side by side[4].

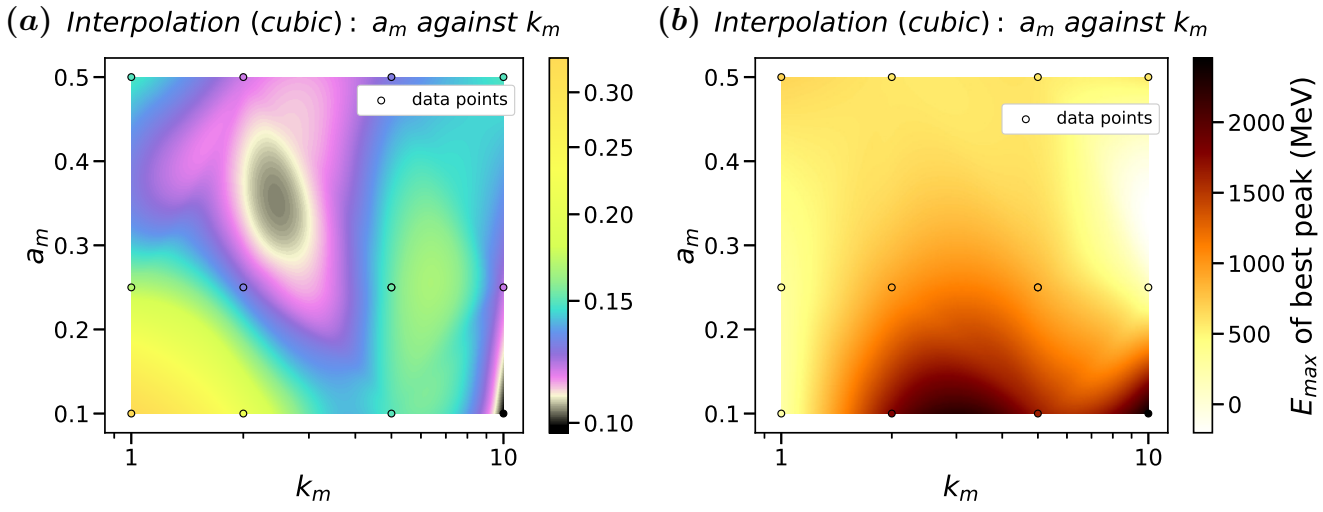

Figure 7: cubic interpolation of the data for the $1\lambda_0$ density modulated target shape: related a_m and k_m with $\Delta E/E_{max}$ $(\boldsymbol{a})$ and E_{max} $(\boldsymbol{b})$ in third dimension.

[4]Notice that for the figures with $\Delta E/E_{max}$, we create this colorbar only for this kind of data, in order to distinguish better the different regions.

In figure 7a, one can see that the best regions for sharp peaks are located in the area where $a_m \approx 0.1$ and $k_m \approx 10$ with $\Delta E_1/E_{max} < 0.10$, followed by $0.3 < a_m < 0.4$ with $2 < k_m < 3$ where $\Delta E_2/E_{max} \in [0.10, 0.11]$. The first area is indeed certain to have low values (see more in figure 13) whereas the second area is defined thanks to the cubic interpolation. To be sure, one can do a simulation in this area to check it[5].

As instability growth is low for low values of $\Delta E/E_{max}$, one can compare the regions with the a_m and k_m from theory. However, for $|k_m a_m| \gg 1$, there is a non-conformity between theory and simulation results. This is due to the fact, that in theory, no modulation in x-direction were considered, the target were assumed to be an ideally reflective target and other approximation should also played a role in this non-conformity. In order to check the reasoning, one can look into the other shapes (where also the right modulation like in theory is displayed).

Concerning figure 7b, one can see, that the maximum reachable energy for the sharpest peaks grow proportionally with a_m and k_m (see figure 22 for more details). This is confirmed with figure 8b. Clearly, one can also see that the exact half of the maximum value of E_{max} from figure 7b is displayed in figure 8b. As the width doubles, one can later see a clean relationship between width and E_{max}.

[5]Notice that the peak for the density modulated targets were not easily obtained. For very low a_m, one had to look manually into the animation and find out the best peaks. For $a_m = 0.01$, no single peaks could be obtained as the whole energy spectrum displays multiple peaks in the nearby region of the dominant peak.

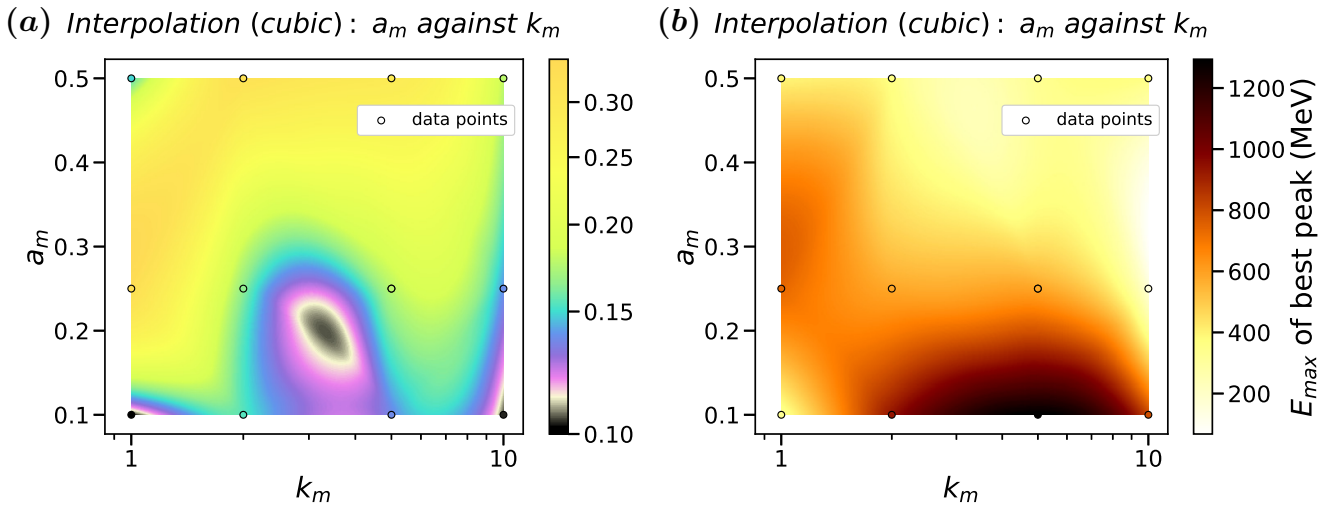

Figure 8: cubic interpolation of the data for the $2\lambda_0$ density modulated target shape: related a_m and k_m with $\Delta E/E_{max}$ $(\boldsymbol{a})$ and E_{max} $(\boldsymbol{b})$ in third dimension.

In figure 8a, a similar behaviour like figure 7a is noticed. However, there seems to be a shift for of the second area with $k_m \rightarrow k_m + 1$ and $a_m \rightarrow a_m - 0.15$. This shift could be dependent on the target width, but this should be checked. In addition, the shift actually impacts also the values $\Delta E/E_{max} \in [0.10, 0.11]$ for $a_m = 0.1$ and $k_m = \{1, 10\}$.

We now show the same plots for the surface modulated targets. These are displayed in figure 9, figure 10 and figure 11. First, it can be seen, that all maximum energy peaks are roughly identical, *i.e* all surface modulated targets have similar values of E_{max} and a clean peak in the ion energy spectrum. However cross-comparing them to the density modulated targets, shows much lower values.

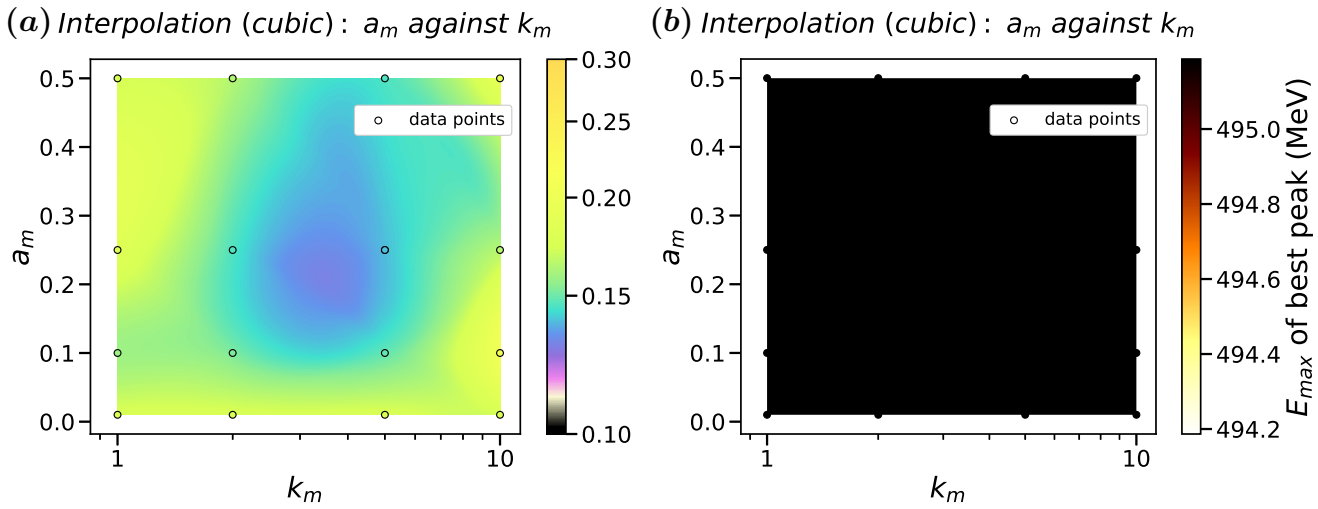

Figure 9: cubic interpolation of the data for the $1\lambda_0$ rec modulated target shape: related a_m and k_m with $\Delta E/E_{max}$ $(\boldsymbol{a})$ and E_{max} $(\boldsymbol{b})$ in third dimension.

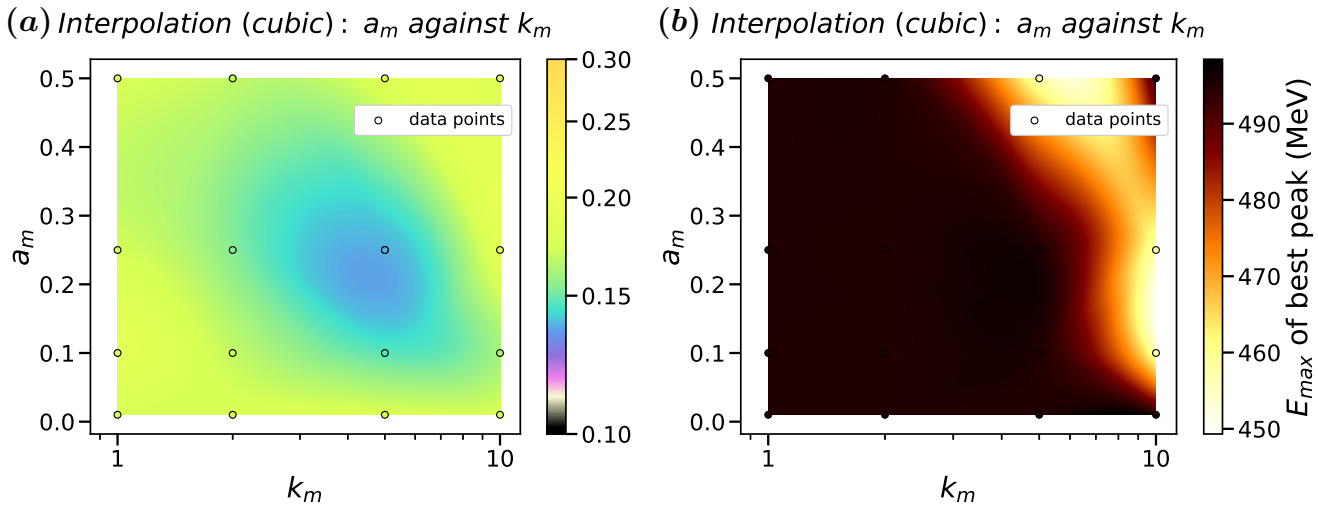

Figure 10: cubic interpolation of the data for the $1\lambda_0$ rp modulated target shape: related a_m and k_m with $\Delta E/E_{max}$ $(\boldsymbol{a})$ and E_{max} $(\boldsymbol{b})$ in third dimension.

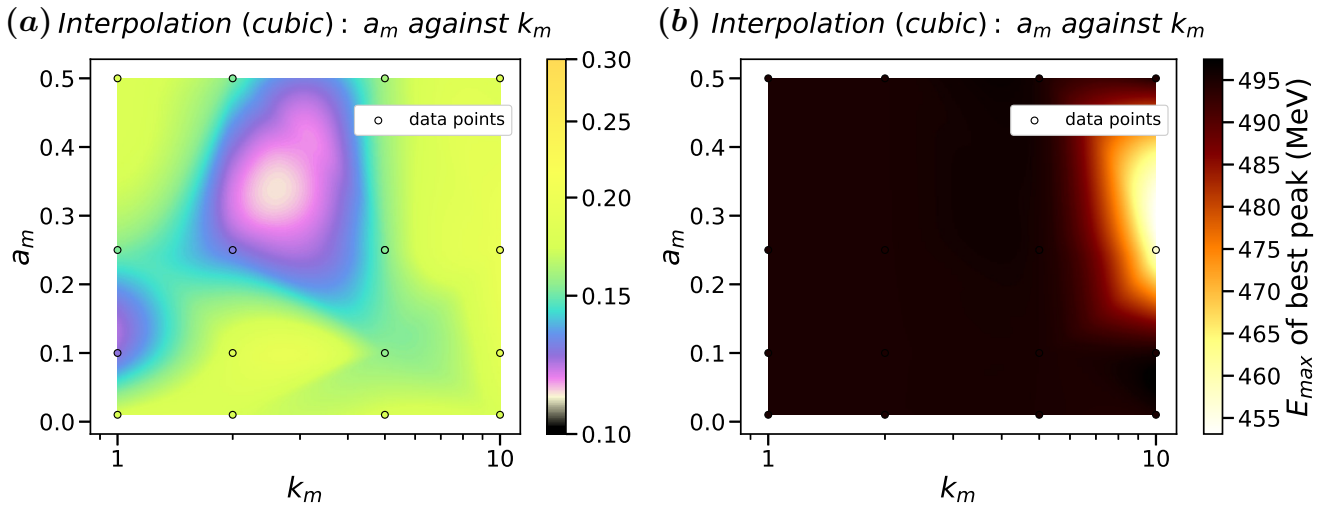

Figure 11: cubic interpolation of the data for the $1\lambda_0$ rpg modulated target shape: related a_m and k_m with $\Delta E/E_{max}$ $(\boldsymbol{a})$ and E_{max} $(\boldsymbol{b})$ in third dimension.

Looking in the $\Delta E/E_{max}$ figures, one can find similar regions for a_m and k_m giving better values of $\Delta E/E_{max}$. The surface modulated target shape that corresponds the best to theory calculations is the rp target. Actually, for this case, only the rippling on the surface is considered. Theory tells, that for values $|k_m a_m| \gg 1$, one can reduce the growth of RTI like instabilities, thus the best results. In figure 10a, this behaviour can be confirmed if the reflectivity of the target is dropped down to 75%. Therefore, the best area would be shifted (for $a_m = 0.25$) from $k_m = 5$ to $k_m = 3$. Thus, the results are according to the expectations.

The other shapes are quite similar. However, the best results for surface modulated targets are obtained for the rpg shape. Here are values of $\Delta E/E_{max} \approx 0.11$, where on the contrary the values $\Delta E/E_{max} \in [0.12, 0.14]$ are obtained for the rec- and rp-shapes.

For a better overview, one needs to cross compare the different values of all maps and display them below:

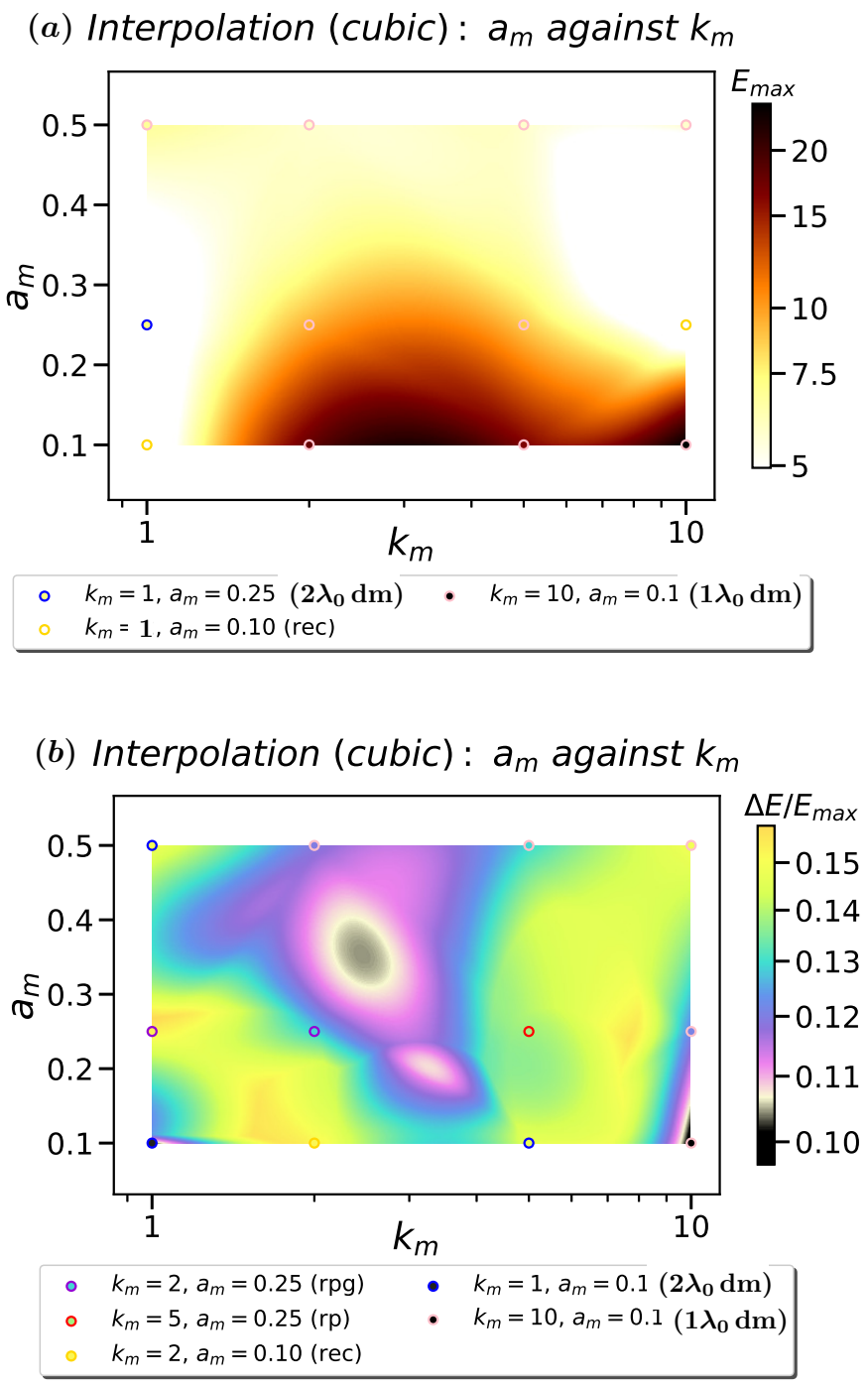

Figure 12: cubic interpolation of the whole data for all target shapes after cross comparing the values of all interpolations: related a_m and k_m with **(a)** E_{max} (in 10^2 MeV) and **(b)** $\Delta E/E_{max}$ in third dimension with best data peaks (color of data points are related to the different shapes).

The two best peaks are thus displayed together with the non-modulated target in figure 13 below.

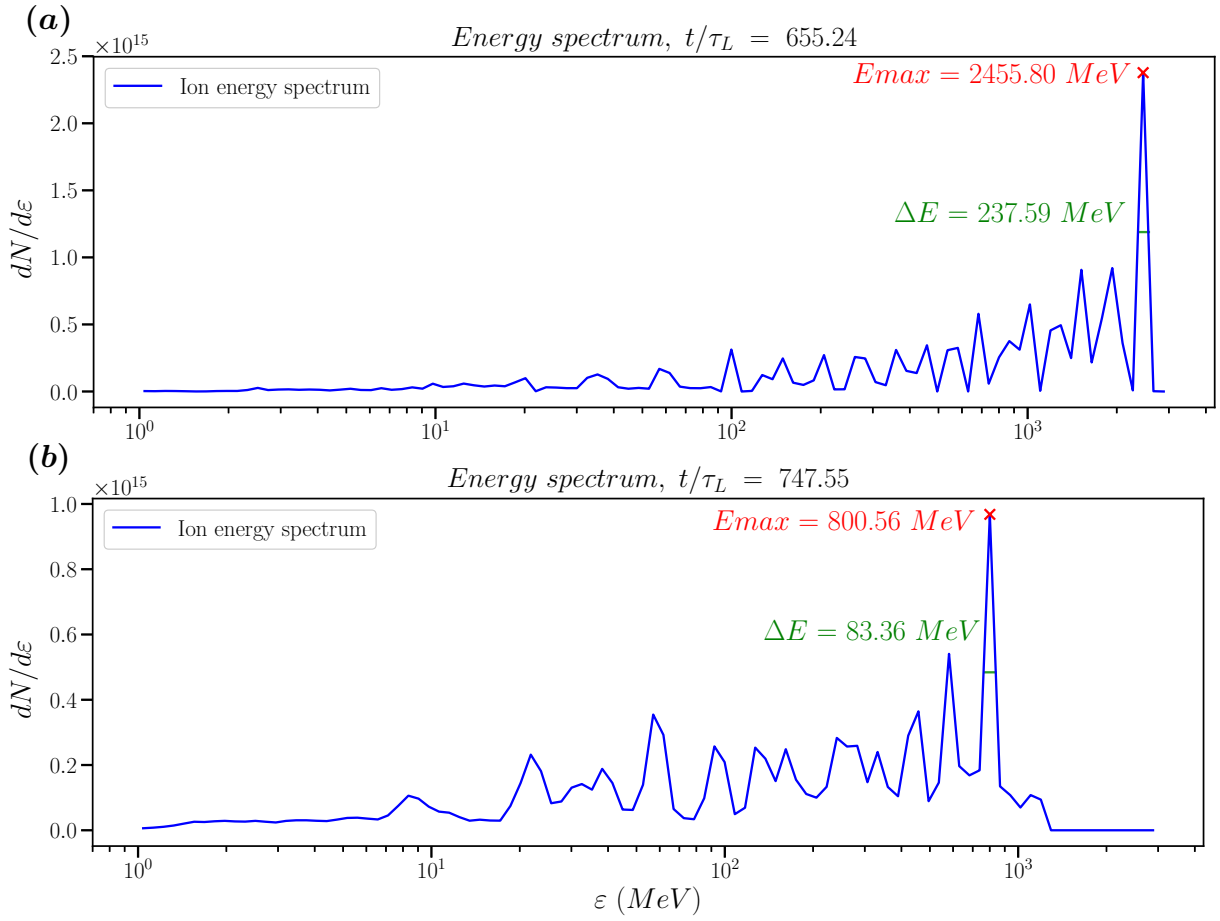

Figure 13: Energy spectrum of **(*a*)** the $1\lambda_0$ and **(*b*)** $2\lambda_0$ density modulated target (both for $k_m = 10$ and $a_m = 0.1$).

The two best peaks are located in the density modulated targets especially for the region $k_m = 10$ and $a_m = 0.1$. Comparing them to figure 4 and figure 14, one can notice, that the amount of particles per energy ($\mathrm{d}N/\mathrm{d}\varepsilon$) is quite low, however one can see that between figure 13a and 13b there is almost a factor of two higher energy in figure 13a compared to figure 13b. The other peaks in the spectra in figure 13 are much sharper than the cluster of peaks in figure 14b in the area

$(1 \times 10^1\,\text{MeV}, 2 \times 10^2\,\text{MeV})$. This could be explained due to heated electrons from the modulated skin-depth layer. In fact, depending on the amplitude and the wave vector of the modulation, one finds different wavelength harmonics in the ion energy spectrum. This is time dependent, as harmonics vary with the position and velocity of the electrons, and therefore, the peak of the RPA ions is unstable in time. This time dependent instability increases for amplitudes less than $a_m < 0.1$. However, these kinds of dominant sharp peaks can be used (as one could select them for specific time steps) and are better than the regular ones (higher energies and lower FWHM) for the surface modulated targets like in figure 4a (which are stable in time). We do a deeper analysis of instabilities later (see section 3.2.3).

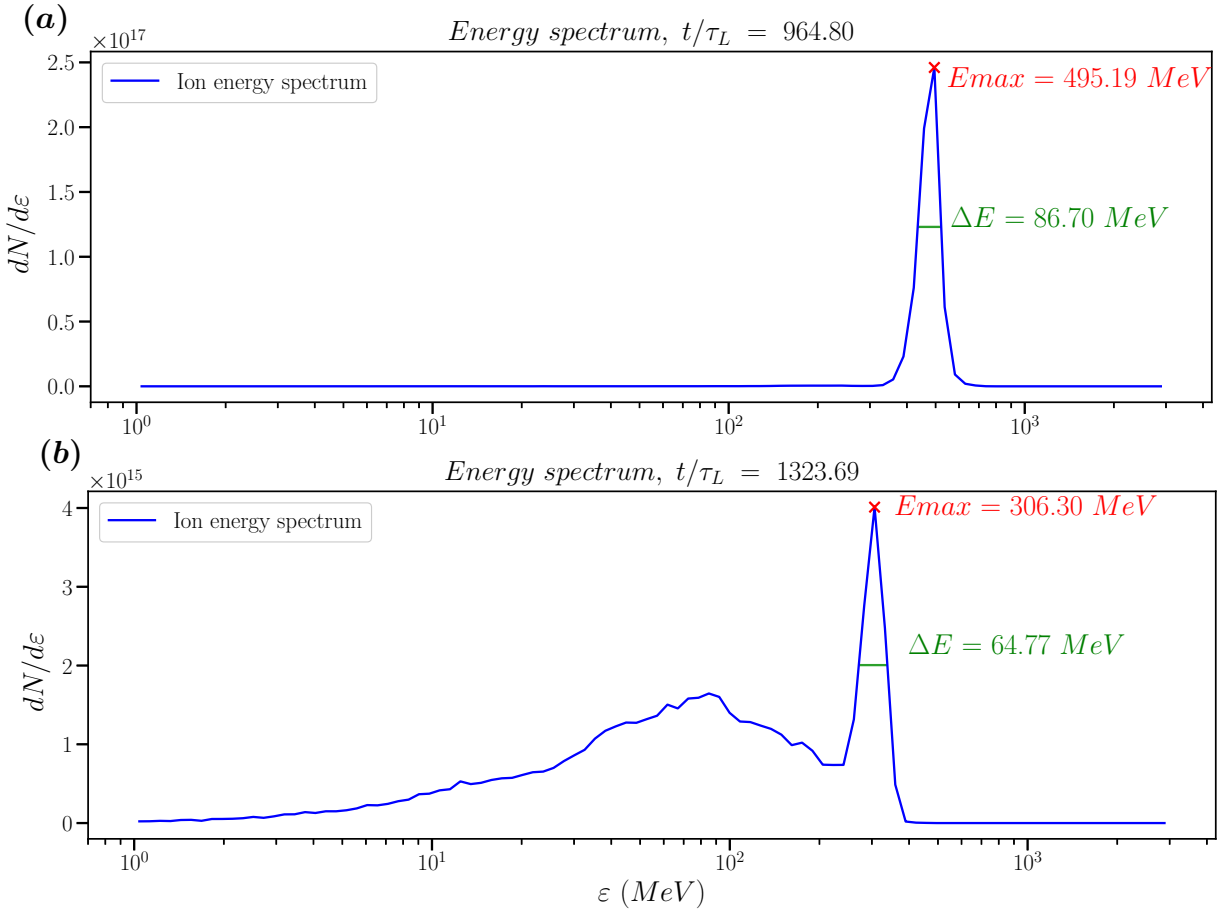

Figure 14: Energy spectrum of **(a)** the $1\lambda_0$ and **(b)** the $2\lambda_0$ non-modulated target.

3.2.3 Instability analysis

In order to understand the instability growth and their development better, we look into the spatial spectra of the ions from which is obtained by taking the Fast Fourier transform (FFT) from the ion density distribution:

$$n(k,t) = \int_0^{L_y} \int_0^{L_x} n(x,y,t) e^{iky} \mathrm{d}x\mathrm{d}y, \tag{72}$$

where $n(k,t)$ is averaged in x-direction and the FFT is taken along the y-direction. Thus, time is plotted against the wave vector based on simulation results (figure 15).

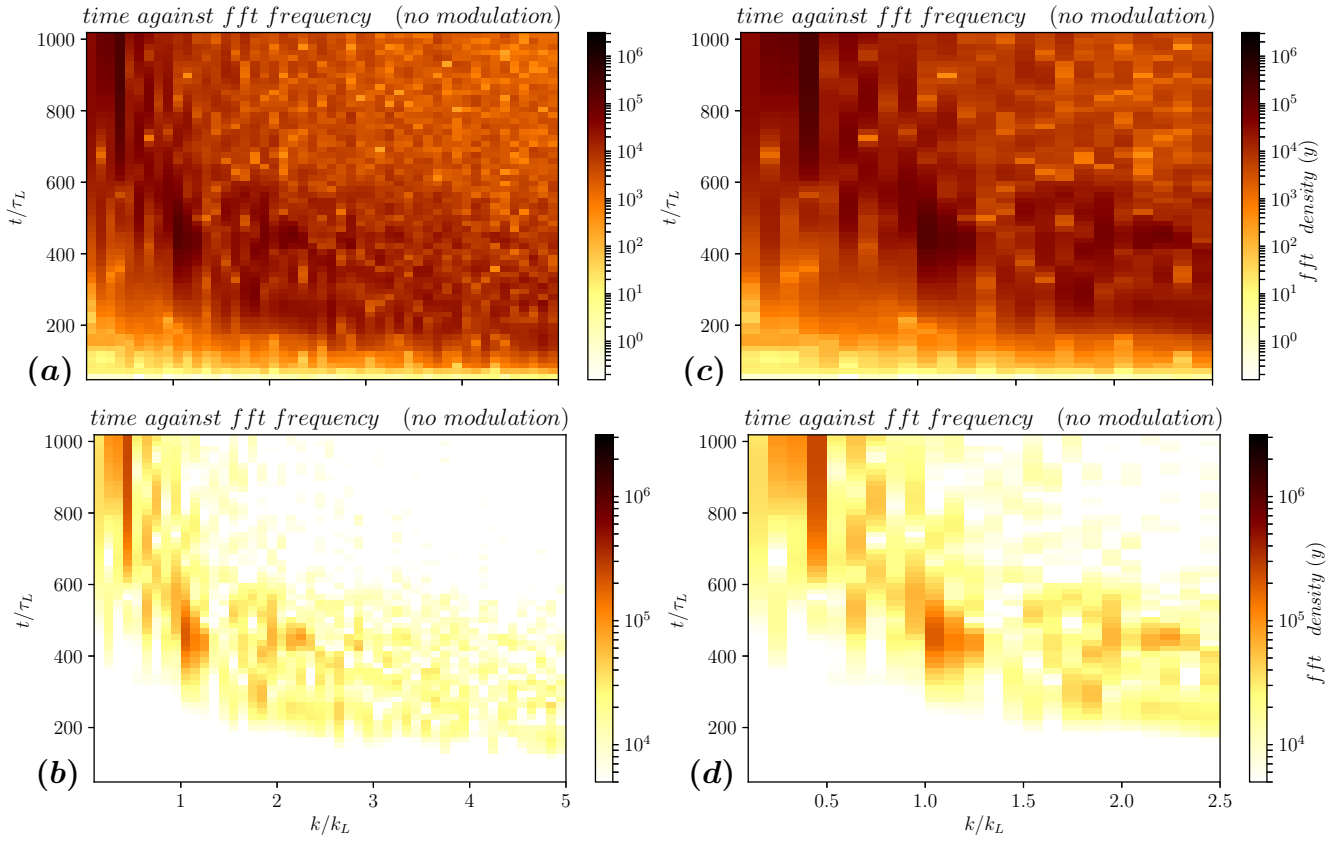

Figure 15: time *i.e* t/τ_L against FFT of the frequency, defined as the normalized wave vector k/k_L with **(*a*)** the whole density behaviour and **(*b*)** selected density intensities in third dimension for the non-modulated target. Same with **(*c*)** and **(*d*)** (zoom).

One can see, that the ion density has modulations in the area where $k/k_L \leq 4$, *i.e* where the wavelength of the instabilities is $\lambda_{inst} \geq 0.25\lambda_0$. As displayed in figure 15d, the dominant mode of the ion density oscillations is located around the area where $\lambda_{inst} \approx \lambda_0$. After the time $t = 600\,\tau_L$, the long wavelengths dominate in time.

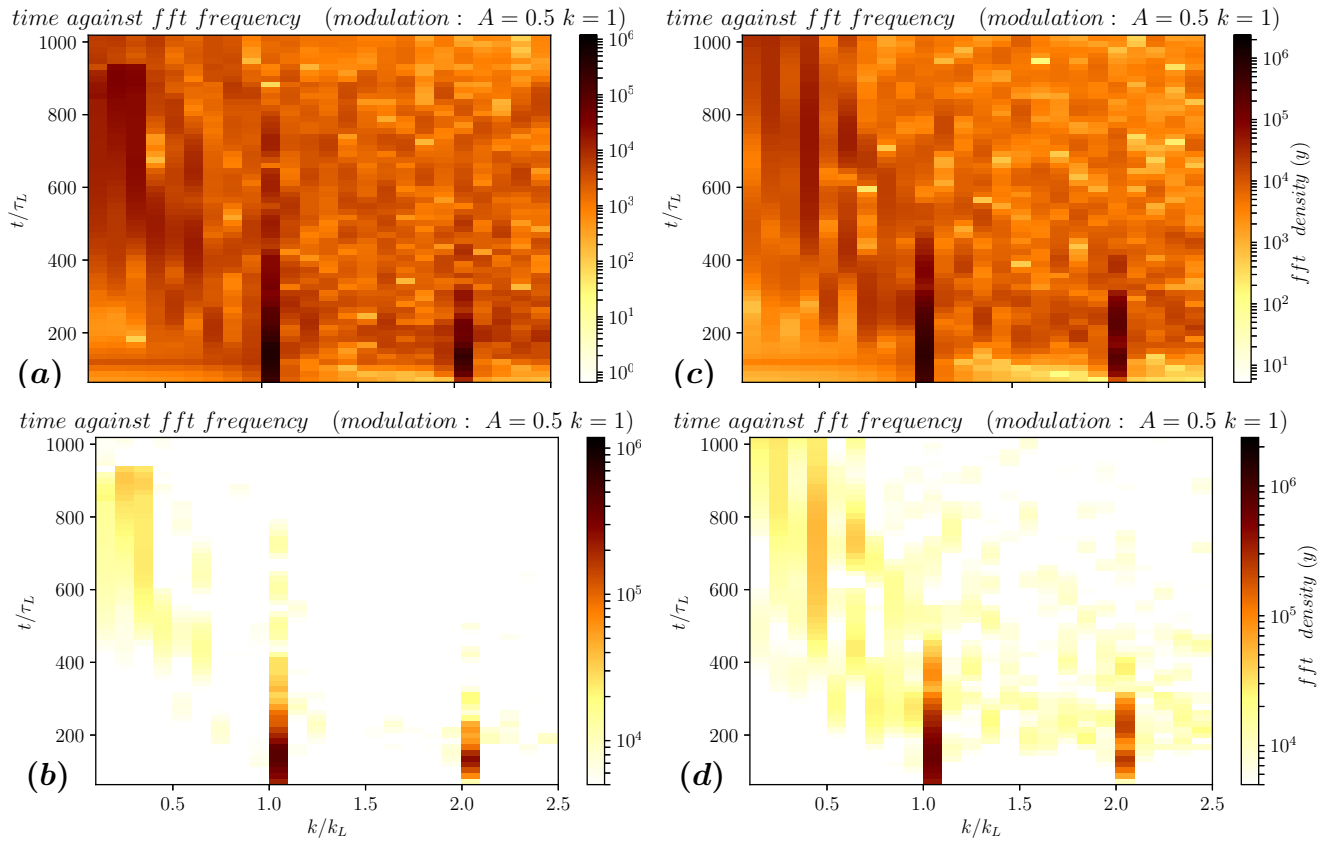

Figure 16: time *i.e* t/τ_L against FFT of the frequency, defined as the normalized wave vector k/k_L with **(*a*)** the whole density behaviour and **(*b*)** selected density intensities in third dimension for the density modulated target with $1\lambda_0$ width and $a_m = 0.50, k_m = 1$. Same for **(*c*)** and **(*d*)** with the $2\lambda_0$ density modulated target.

In figure 16, one can see that the amplitude of the density is slightly lower for the $1\lambda_0$ width than the $2\lambda_0$ width modulation and the long wavelengths dominate much earlier for the $2\lambda_0$ case and continue for a longer time period. The ideal case to achieve is a have instability modes with shorter wavelength in order to stabilize the

RPA, as long wavelengths of the instability cause breaking of the target. Actually, the behaviour of the instability modes *i.e* the stabilization of the instability occurs *i.a* due to the transverse ion motion and diffusion of the target mass. Thus, the $1\lambda_0$ density modulated target have better results than the $2\lambda_0$ case.

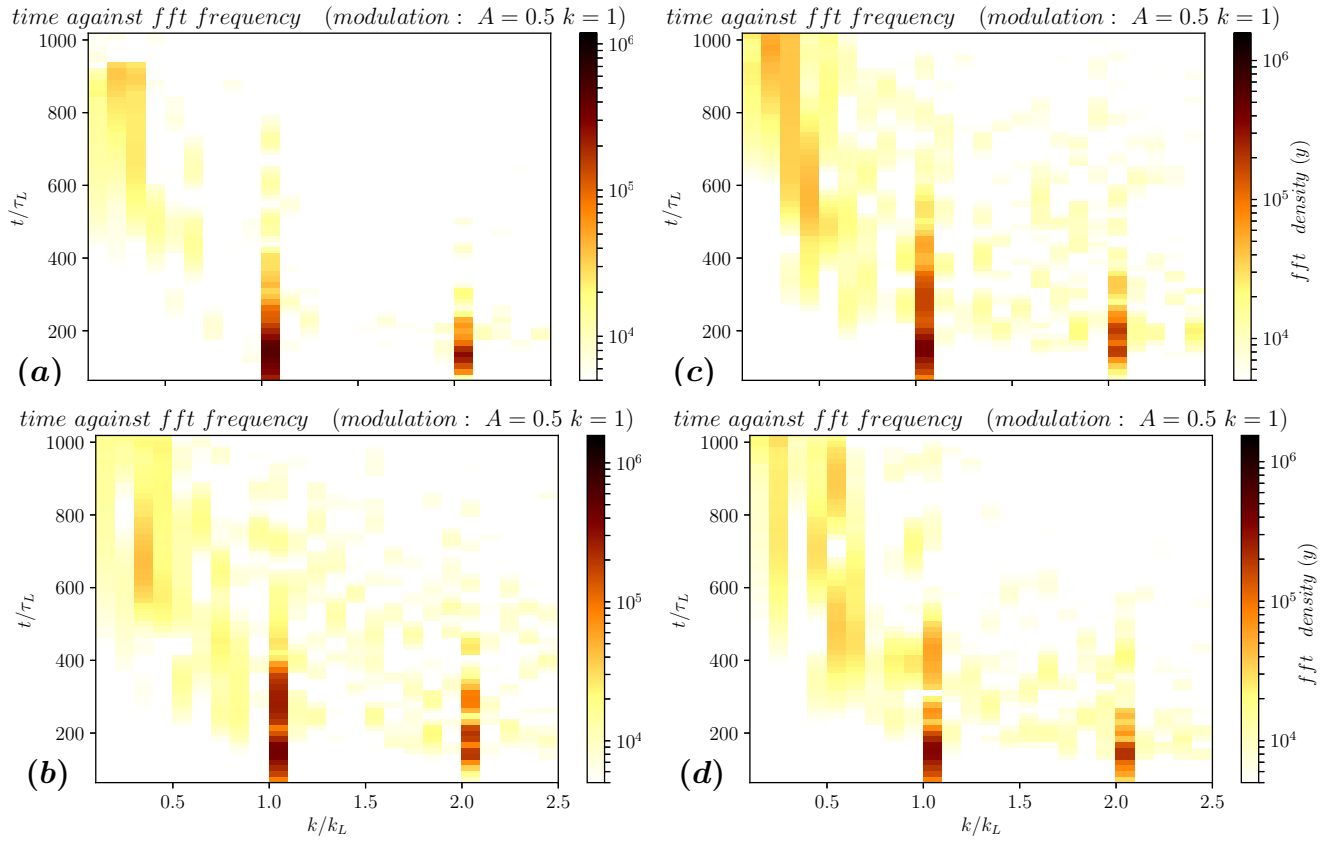

Figure 17: time *i.e* t/τ_L against FFT of the frequency, defined as the normalized wave vector k/k_L with the selected density behaviour in third dimension and $a_m = 0.50, k_m = 1$ for **(a)** the density modulated target ($1\lambda_0$-width), **(b)** the rp surface-modulated target, **(c)** the rec surface-modulated target and **(d)** the rpg surface-modulated target.

For a modulated target (for a modulation wavelength of $1\lambda_0$ in figure 16 and figure 17[6]), a reduction of the spectra and amplitude of instability modes can be

[6]the whole density behaviour is in appendix

observed. For the different $1\lambda_0$ width modulations, the long wavelengths dominate at much later time $t = 400\,\tau_L$ or $t = 600\,\tau_L$, depending on the modulation.

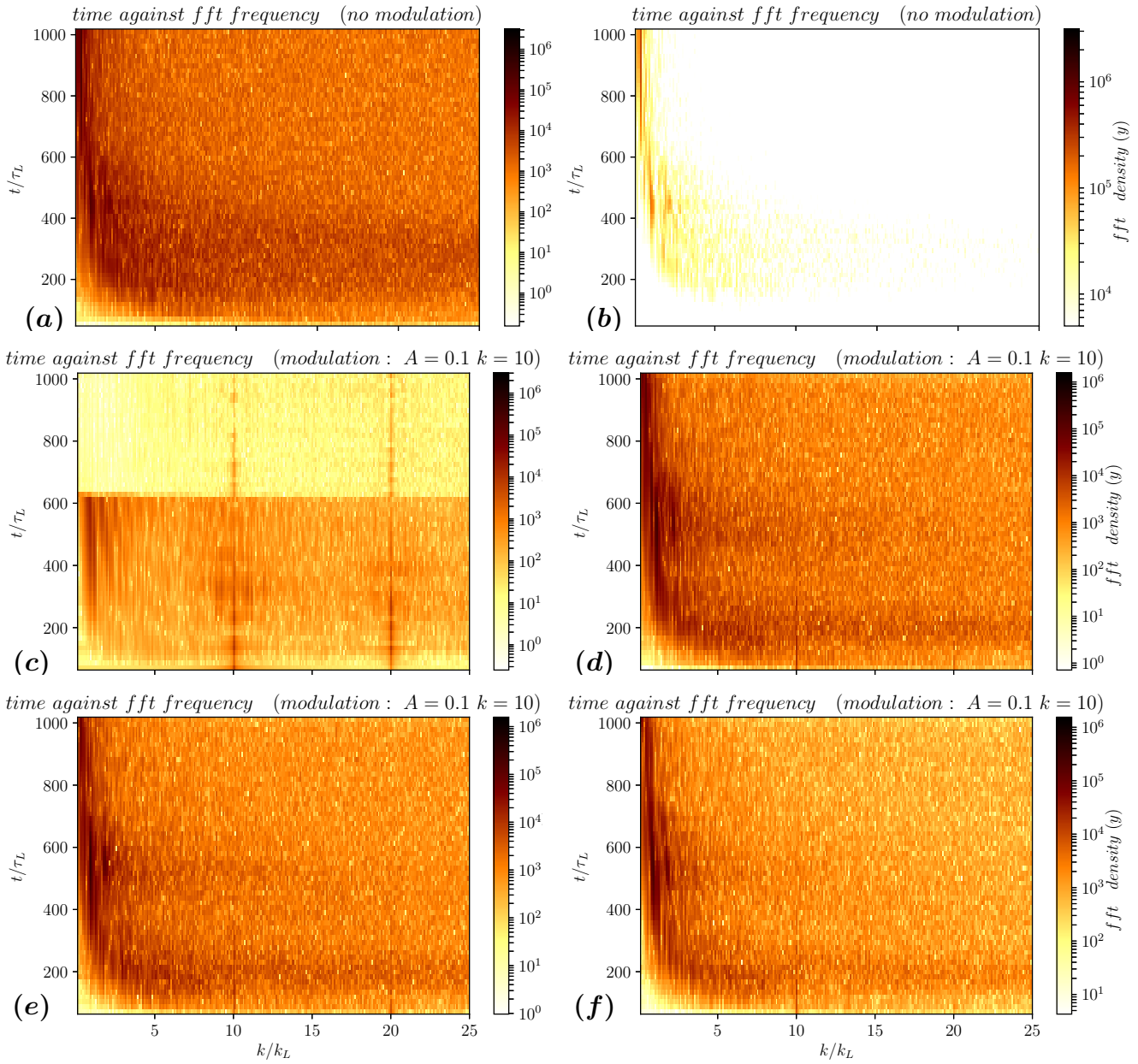

Figure 18: time *i.e* t/τ_L against FFT of the frequency, defined as the normalized wave vector k/k_L for **(*a*)** the non-modulated target, **(*b*)** selected intensities for the non-modulated target, **(*c*)** the dm modulation, **(*d*)** the rec modulation, **(*e*)** the rp modulation and **(*f*)** the rpg modulation (all have a $1\lambda_0$ width).

However, the long wavelength perturbations have globally much lower amplitude for the modulated than for the non-modulated targets. The reduction or rather suppression of the low instability modes (*i.e* long wavelength perturbations) is also been observed in figure 18: All the surface modulations have the dominant mode of the ion density oscillations near the area where $\lambda_{inst} \approx 0.10\lambda_0$. For the density modulated target, these modes are stronger than the long wavelengths until the time $t \approx 300\,\tau_L$. This is due to the recently explained effect of electrons reaching faster the back of the target thanks to the modulation of the plasma density.

One can also notice, that for the $1\lambda_0$ density modulated target, the long wavelength in figure 18c stopped around $t \approx 600\,\tau_L$, this behaviour is also observed in figure 16b but for $t \approx 900\,\tau_L$. This can be explained by a loss of the target mass in longitudinal direction into the vacuum. This is actually the TNSA-regime. One now have a hybrid regime of TNSA and RPA, but the RPA-regime dominates in this case.

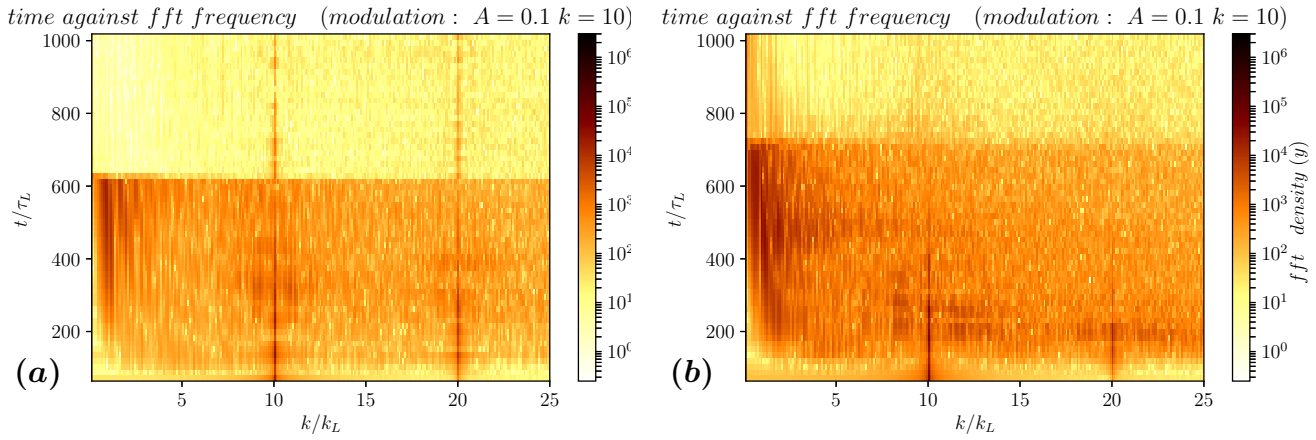

Figure 19: time *i.e* t/τ_L against FFT of the frequency, defined as the normalized wave vector k/k_L with the whole density behaviour for the density modulated targets with **(*a*)** $1\lambda_0$ width and **(*b*)** $2\lambda_0$ width.

Comparing figure 19a and 19b, one can see a different amplitude of the instability

modes. As the $1\lambda_0$ density modulated target has less target mass and is smaller in x-direction, this target has less ion density modulation and enters faster into the hybrid regime (the time at which FFT amplitude is low starts sooner) than the $2\lambda_0$ density modulated target.

Notice, that the best results for the density modulated targets are obtained for times after the loss of the target mass. The instability modes in higher order persist (especially for the $1\lambda_0$ density modulation), and the long wavelength modes no longer play a role in RPA of ions (see figure 19).

The phase space of the target shapes are plotted in order to get an idea where the ions reach a stable velocity. In figure figure 20e, one can see that this is the case for $x \geq 95\lambda_0/2\pi$. The other cases are displayed in figure 20 and figure 21.

Most of the surface-modulations have a linear phase space between $-250\, m_e c < p_x < 1000\, m_e c$. However, the majority of the forward moving ions have all a constant velocity at the end of the simulation box. Without the moving window (*i.e* the target is not tracked after it leaves the simulation box), one could find negative momentum of ions in some phase space regions. This could be explained with a loss of ions from the foil in the front side where the laser hits the target. Actually, these ions are detached from the target surface due to plasma dynamics displayed in figure 22 showing vortex formations. Then, the lost ions don't manage to keep up with the moving foil. This process should however be more analyzed in-depth and leads to a new explorable research area.

The thickness of the lines in the phase space and the density of ions are proportional to the number of particles in the ion energy spectra. All cases do not have the plateau (like figure 20e) in the same x-position. This depends on the configuration of the target shapes and modulations.

The behaviours of the phase space in figure 21a and figure 21b are however special cases: Here one cannot find a constant momentum for cases of unstable ion energy spectra (the plateau could be displayed outside the simulation box).

For the surface-modulated targets in figure 21, one can see an unstable region before the plateau and a split of two dominant ion populations which merge again. The laser pulse accelerates the ions with a higher efficiency due to surface modulations which have higher absorption of the laser pulse than the target without modulation. The rippling in the surface modulation in fact is reflected in the rippled line of the momentum (seen in all figures, but mostly observed in figure 20).

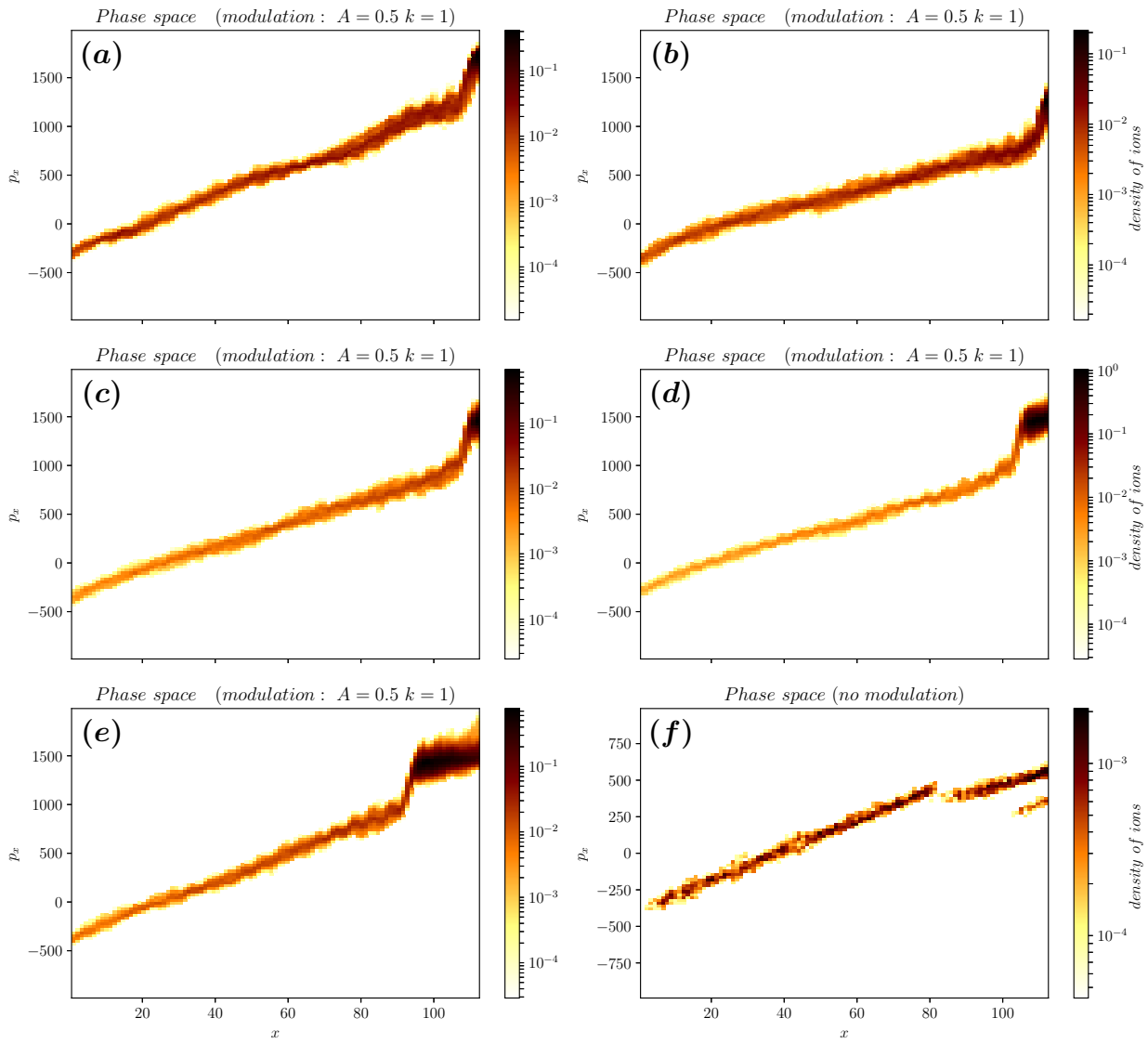

Figure 20: Phase space of the $1\lambda_0$ dm modulation. x is in dimension of $\lambda_0/2\pi$ and momentum p_x is normalized with $m_e c$ for $a_m = 0.50$ and $k_m = 1$ with **(*a*)** the density modulated target ($1\lambda_0$ width), **(*b*)** the density modulated target ($2\lambda_0$ width), **(*c*)** the rec surface-modulated target, **(*d*)** the rpg surface-modulated target, **(*e*)** the rp surface-modulated target and **(*f*)** the non-modulated target

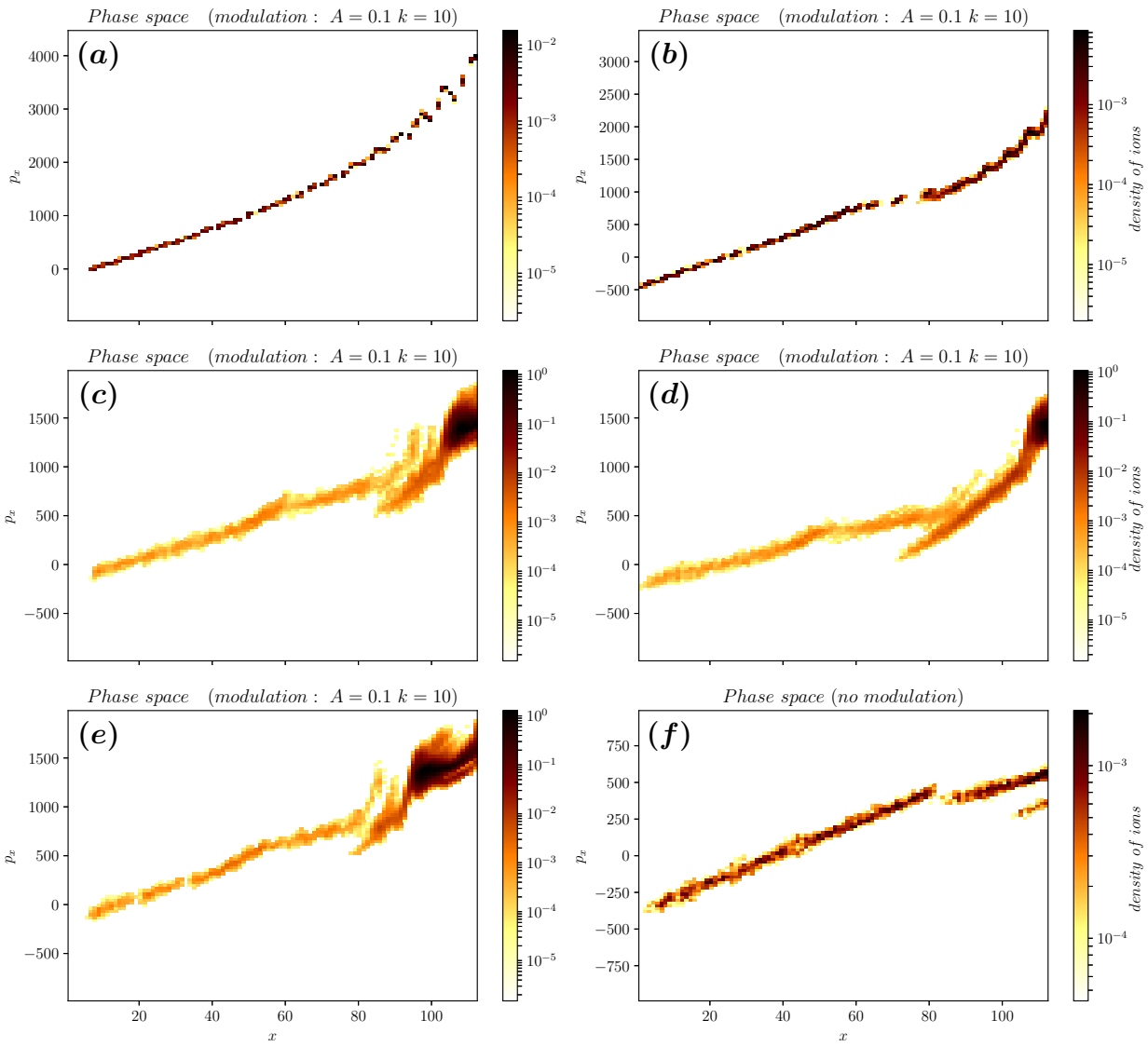

Figure 21: Phase space of the $1\lambda_0$ dm modulation. x in dimension of $\lambda_0/2\pi$ and momentum p_x is normalized with $m_e c$ for $a_m = 0.10$ and $k_m = 10$ with **(*a*)** the density modulated target ($1\lambda_0$ width), **(*b*)** the density modulated target ($2\lambda_0$ width), **(*c*)** the rec surface-modulated target, **(*d*)** the rpg surface-modulated target, **(*e*)** the rp surface-modulated target and **(*f*)** the non-modulated target

3.2.4 Further analysis

In order to foresee the behaviours of other simulations (especially to know also how it depends for different target-widths), we try to get a relation between the target and modulation shape or rather its length, a_m, k_m and the E_{max} maximum energy reachable for the sharpest peaks.

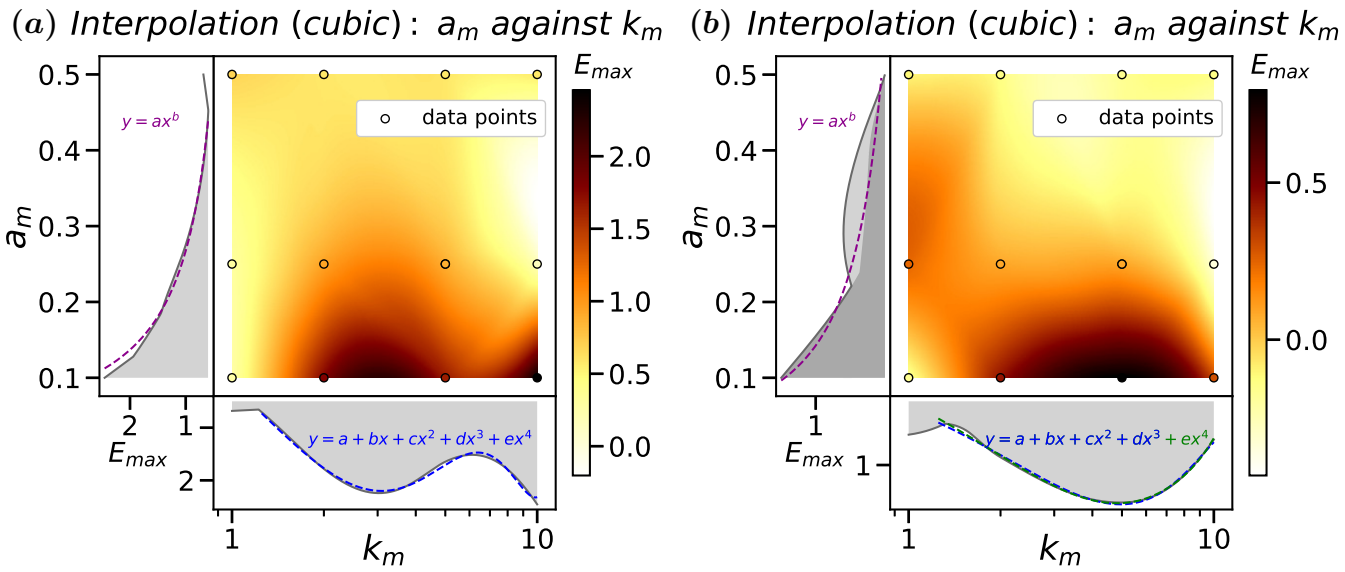

Figure 22: cubic interpolation of the data from density modulated targets: related a_m and k_m with E_{max} (in 10^2 MeV) in third dimension for **(*a*)** $1\lambda_0$ and **(*b*)** for the $2\lambda_0$ widths.

The figures 7b and 8b are analyzed in-depth, where k_m and a_m are plotted against E_{max} separately (see figure 22). In figure 22b, we can eliminate the light gray area in the plot a_m against E_{max}, as we are supposed to have a continuous line. Furthermore, also the plot of k_m against E_{max} does not include the value of $k_m = 1$. That is why, we will only use values where $k_m \gtrsim 1.5$. In addition, one can see, that different fits are displayed in the figures, which are useful for deducing the relation of E_{max}.

Assuming, that the modulation has a non-modulated target length of ℓ and a

modulation length of ℓ_{mod} (so the total target length is $L = \ell + \ell_{mod}$) and supposing that the surface modulated targets have similar behaviours, *i.e* have a nearly constant value of E_{max} for amplitudes $a_m \ll L$ (that is almost the case, comparing the different data values of the $L = 1\lambda_0$ case), one can plot:

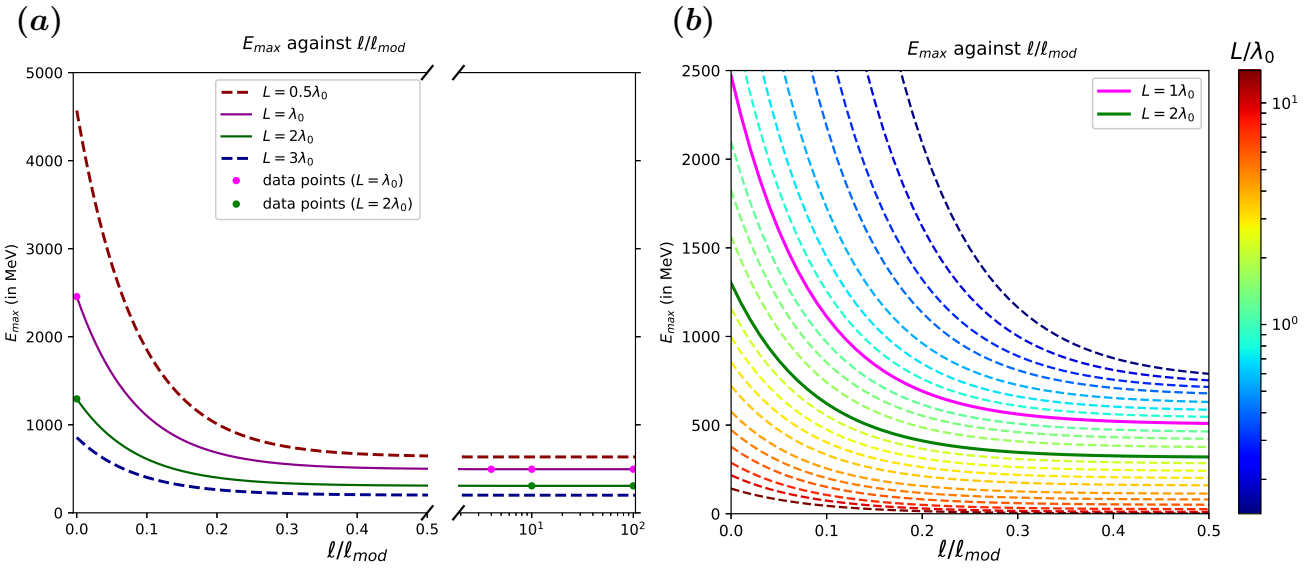

Figure 23: E_{max} against ℓ/ℓ_{mod} with **(*a*)** the fits with the data points and **(*b*)** behaviour for other target widths.

The green line is plotted, supposing that the surface modulated target has the same behaviour for the $2\lambda_0$ target width *i.e* it has the same reachable maximum energy E_{max} like the non-modulated target. This assumption is valid as this behaviour was observed for the $1\lambda_0$ target width and simulations are consistent. The fit function of an exponential decay was chosen as the data points are widely spread (up to $\ell/\ell_{mod} = 100$) and only the exponential function fits with this kind of data.

The fit coefficients can therefore be used to describe the relation of E_{max} as follows:

$$
\begin{aligned}
E_{max} &= E_{max}(\ell, \ell_{mod}, \lambda_0, a_m, k_m), \\
E_{max} &= C_1 E_{\ell_{mod} \ll \ell} + C_2 E_{\ell \ll \ell_{mod}} \cdot \exp\left(-\beta \frac{\ell}{\ell_{mod}}\right), \\
E_{max} &\simeq \alpha^{\frac{L}{\lambda_0}} E_{\ell_{mod} \ll \ell} + \frac{C_2 \lambda_0}{\ell_{mod}} a_m^{-\alpha} P(k_m, \ell_{mod}) \cdot \exp\left(-\beta \frac{\ell}{\ell_{mod}}\right).
\end{aligned} \tag{73}
$$

where $\alpha = 0.63$ is a constant where we can also assume, (for the value of $\alpha^{\frac{L}{\lambda_0}}$) that the ideal target has $L \to 0$ where $L = \ell + \ell_{mod}$ is the total target length, $E_{\ell_{mod} \ll \ell} = 800$ MeV, $C_2 E_{\ell \ll \ell_{mod}} = 1967\,(\ell_{mod}/\lambda_0)$ MeV, $\beta = 11.75$ is a constant, a_m is the amplitude of the modulation, k_m is the wave vector of the modulation, λ_0 is the laser wavelength and P is a polynomial function.

The factor of $\alpha^{\frac{L}{\lambda_0}}$ was chosen, as the minimum E_{max} varies with L. With this result, $E_{\ell_{mod} \ll \ell} = 800$ MeV could be obtained. Thus, $C_1 E_{\ell_{mod} \ll \ell}$, the minimal value of the exponential decay is only related to ℓ as amplitude and the wave vector did not change this value (see data points for the $\ell = \lambda_0$ case).

The other exponential coefficients are more difficult to obtain. However, as the maximum energy doubles when going from the $2\lambda_0$ to the $1\lambda_0$ case, one can write a proportional relation like $E_{\ell \ll \ell_{mod}} \propto \lambda_0/\ell_{mod}$. The value of β is already taken from the two fits in figure 23 (fortunately, both fits showed the same value of β with a deviation of 0.01), supplemented with the x value ℓ/ℓ_{mod} of the plot. Last but not least, from the fits in figure 22, one can include the relation of E_{max} with a_m and k_m, where $a_m^{-\alpha}$ is taken from the fit parameters of $y = a \cdot x^b$ with a a constant included in C_2. Finally, k_m is included with the polynomial function $P(k_m, l_{mod})$ which is dependent on ℓ_{mod} as different coefficients are obtained for the two different modulation lengths for the fits in figure 22.

Therefore, for a $3\lambda_0$ density modulated target, we expect for best a_m and k_m parameters a maximum value of $E_{max} \simeq 0.63^3 \times 800\,\text{MeV} + \frac{1}{3}\,1967 \times \exp(-11.75 \cdot 0)\,\text{MeV} = 856\,\text{MeV}$. In the other region, where $\ell \gg \ell_{mod}$ *i.e* for surface modulated targets, one will find a $E_{max} \simeq 0.63^3 \cdot 800\,\text{MeV} + \frac{1}{3}\,1967 \cdot \exp(-11.75 \times 100)\,\text{MeV} \simeq 0.63^3 \cdot 800\,\text{MeV} = 200\,\text{MeV}$. The dark blue line in figure 23a displays the behaviour of E_{max} for this case. Analogically, one can do the same for other target thicknesses (for example the dark red dashed line for a $L = 0.5\lambda_0$ thickness).

Generally, one can see with figure 23 and equation 73 that the best results, *i.e* the maximum E_{max} can be obtained for density modulated targets (dm modulations) with a target thickness of $L = \ell_{mod} \to 0$ (however, we did not consider the effect of the BOA-regime if the skin-depth layer is too small) and with a modulated density amplitude inside the target of $a_m \leq 0.1$. Like before, all cases of density modulated density (dm) have a maximum density of $a_{m_{max}} = a_m$ and a minimum density of $a_{m_{min}} = 0.5\,a_m$ inside the target (see also figure 1d).

4 Conclusions and Discussions

A stabilized RPA has been a long standing goal in these research areas. The goal to obtain a reduction of the RTI-like instabilities in order to get a peak with sharpness of $\Delta E/E_{max} = 0.05$ for tumor therapy will still have a long way ahead. However with our modulation shapes, one gets values of $\Delta E/E_{max} \approx 0.097$ which is very promising.

Studying density modulated target target shapes turned out to have a great potential in RPA as these modulation shapes realized much better results than surface-modulated targets. In fact, the broadening of the peaks in the ion energy spectrum are minimized even if these peaks are very unstable in time for extremely low modulation amplitude values.

For density modulated targets, the instability growth for long wavelength can be very interesting. Actually, the beginning of a RPA-TNSA hybrid-regime is very promising due to the loss of long wavelength instability modes in the modulated ion density. This allows the unstable time development of sharp peaks in the ion energy spectra with a suppressed instability growth (figure 19).

The simulation data also revealed a relation between modulation parameters and the maximum value of the dominant peaks in the ion energy spectra. This allows further a description of the behaviour between energy peaks, target thickness and modulation parameters for next simulations.

In order to improve PIC-simulations, one needs to adapt theory calculations for the density modulated targets by including the variation in the radiation pressure due to the pre-imposed surface and density modulations. Furthermore, our next step is to extend our research in considering the radiation reaction process and to look into these new simulations in order to see how radiation reaction will affect the results. One can, in addition, modulate the laser shapes and consider also Gaussian

or semi-Gaussian laser shapes.

5 Outlook

5.1 Influence of Radiation Reaction of the RPA of ions for surface/density modulated targets

We performed one simulation of the best peaks from previous results and included the radiation reaction (RR) force with $a_0 = 250$ instead of $a_0 = 150$.

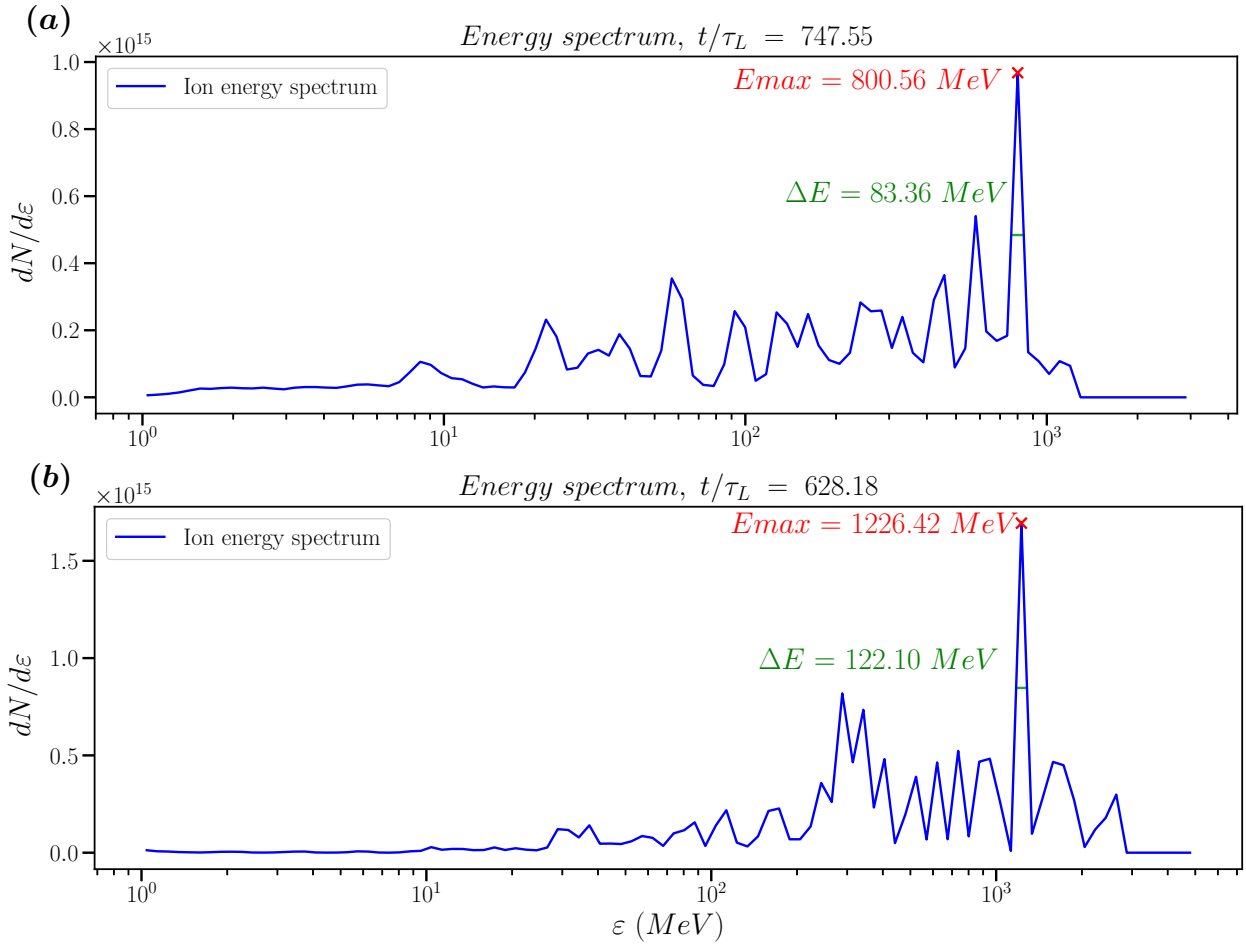

Figure 24: Energy spectrum of the $2\lambda_0$ density modulated target at $k_m = 10$ and $a_m = 0.10$ and **(a)** $a_0 = 150$, **(b)** $a_0 = 250$.

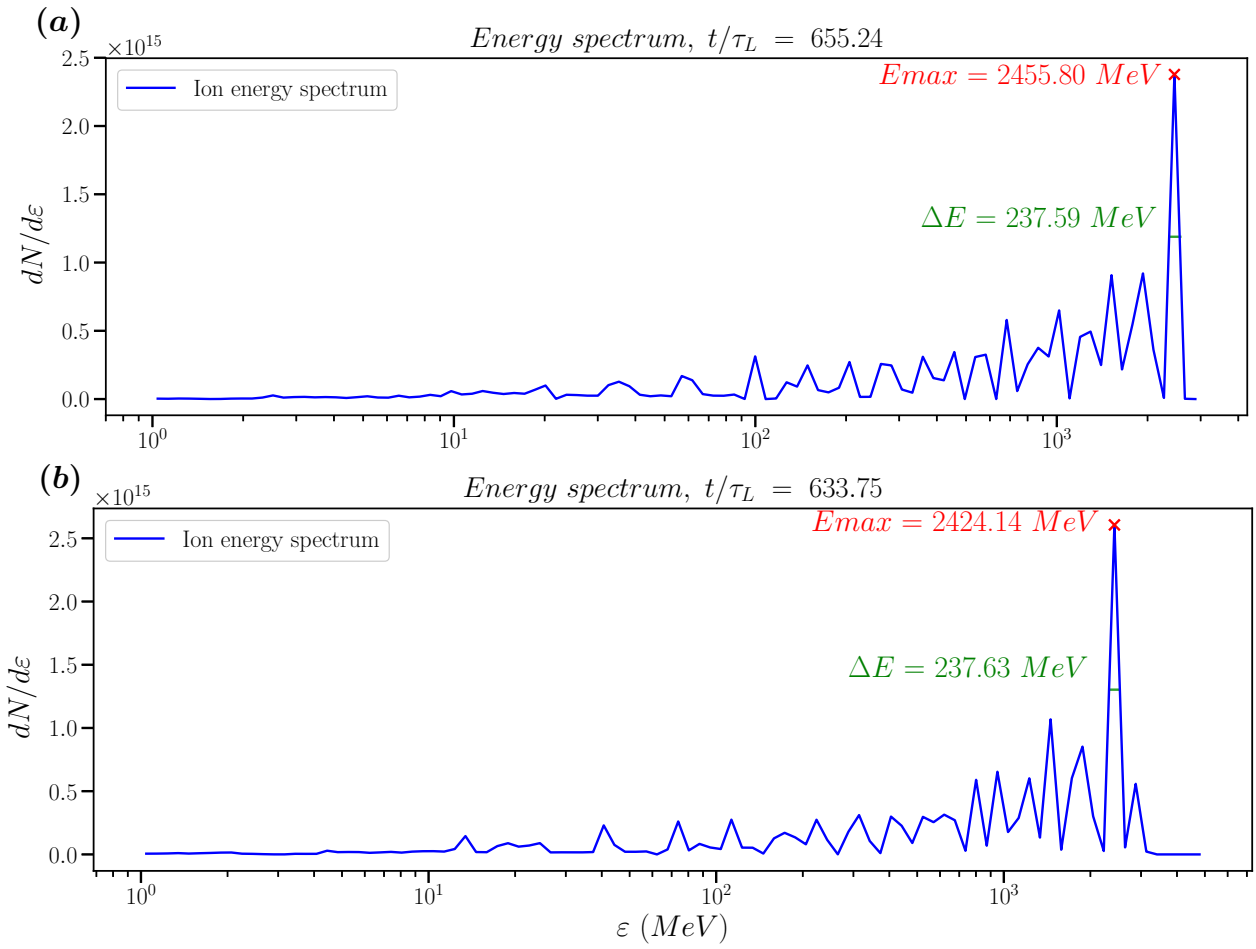

Figure 25: Energy spectrum of the $1\lambda_0$ density modulated target at $k_m = 10$ and $a_m = 0.10$ and **(*a*)** $a_0 = 150$, **(*b*)** $a_0 = 250$.

Here, globally one cannot reach lower values of $\Delta E/E_{max}$. The energy spectra have similar peaks like in earlier simulations. Due to the radiation reaction (RR), one expects that the peaks in the ion energy spectra should be more suppressed, and therefore should have lower energy. This behaviour is however not observed. RR is so weak for our parameters, that it does neither affect significantly the particle number in the energy spectra nor the peak width. For density modulated targets, one has, if anything, a slightly higher amount of particles. The sharpness of the peaks vary and no trend could be observed, *i.e* values with RR

and without RR are quite similar as $(\Delta E/E_{max})_{RR,1\lambda_0} > (\Delta E/E_{max})_{no\,RR,1\lambda_0}$ and $(\Delta E/E_{max})_{RR,2\lambda_0} < (\Delta E/E_{max})_{no\,RR,2\lambda_0}$ due to the unstable energy spectra in time.

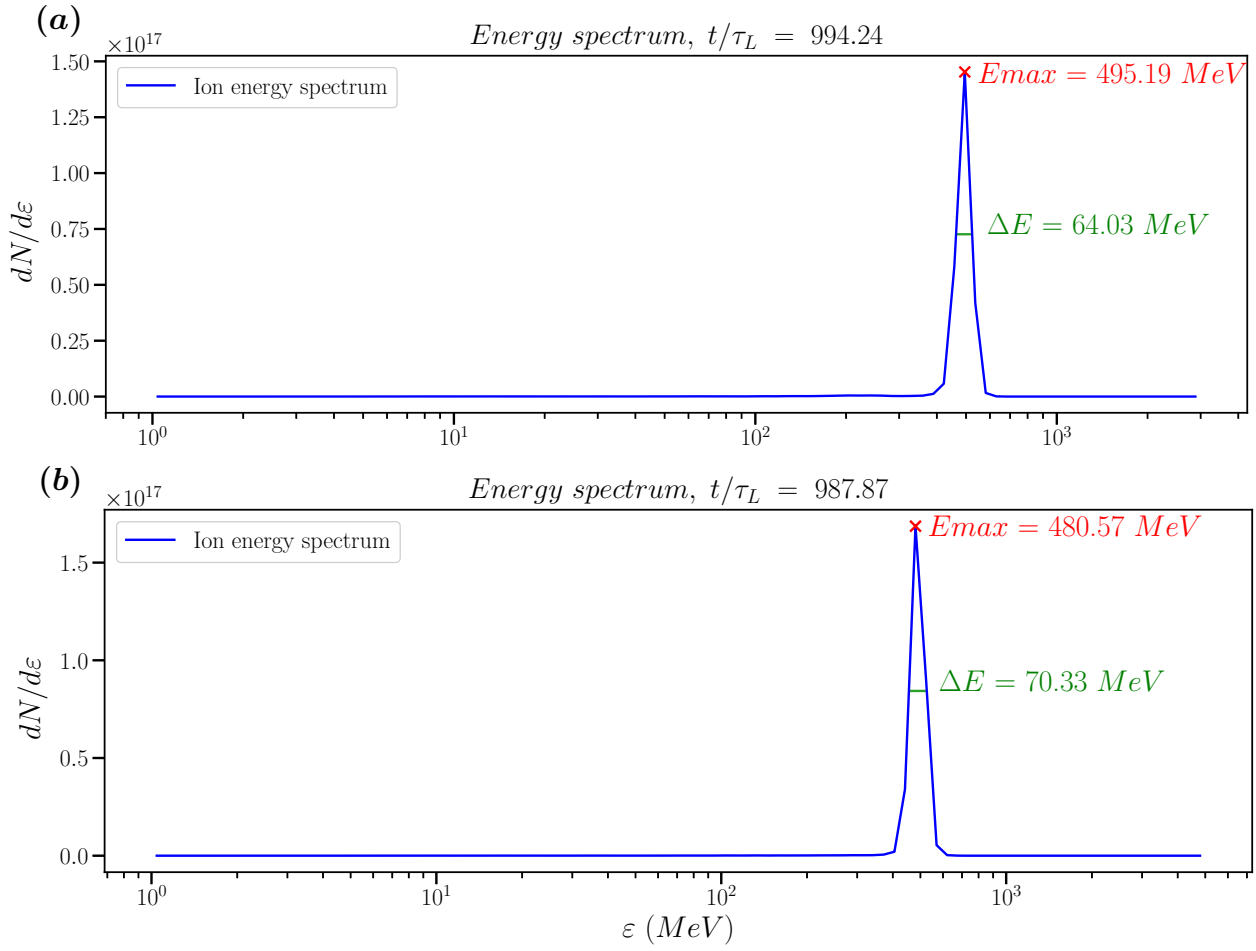

Figure 26: Energy spectrum of the rpg modulated target at $k_m = 1$ and $a_m = 0.5$ and **(a)** $a_0 = 150$, **(b)** $a_0 = 250$.

For surface modulated targets, this behaviour is also present. Thus, with RR, the sharpness of the peak leads to a little augmentation of $\Delta E/E_{max}$ by around 1% to 2% for surface modulated targets (see figure 26. Other surface modulations have similar behaviours). Therefore, apart from reaching the hybrid regime sooner for figure 27h, one can see that RR is not so relevant for modulated targets in ion RPA.

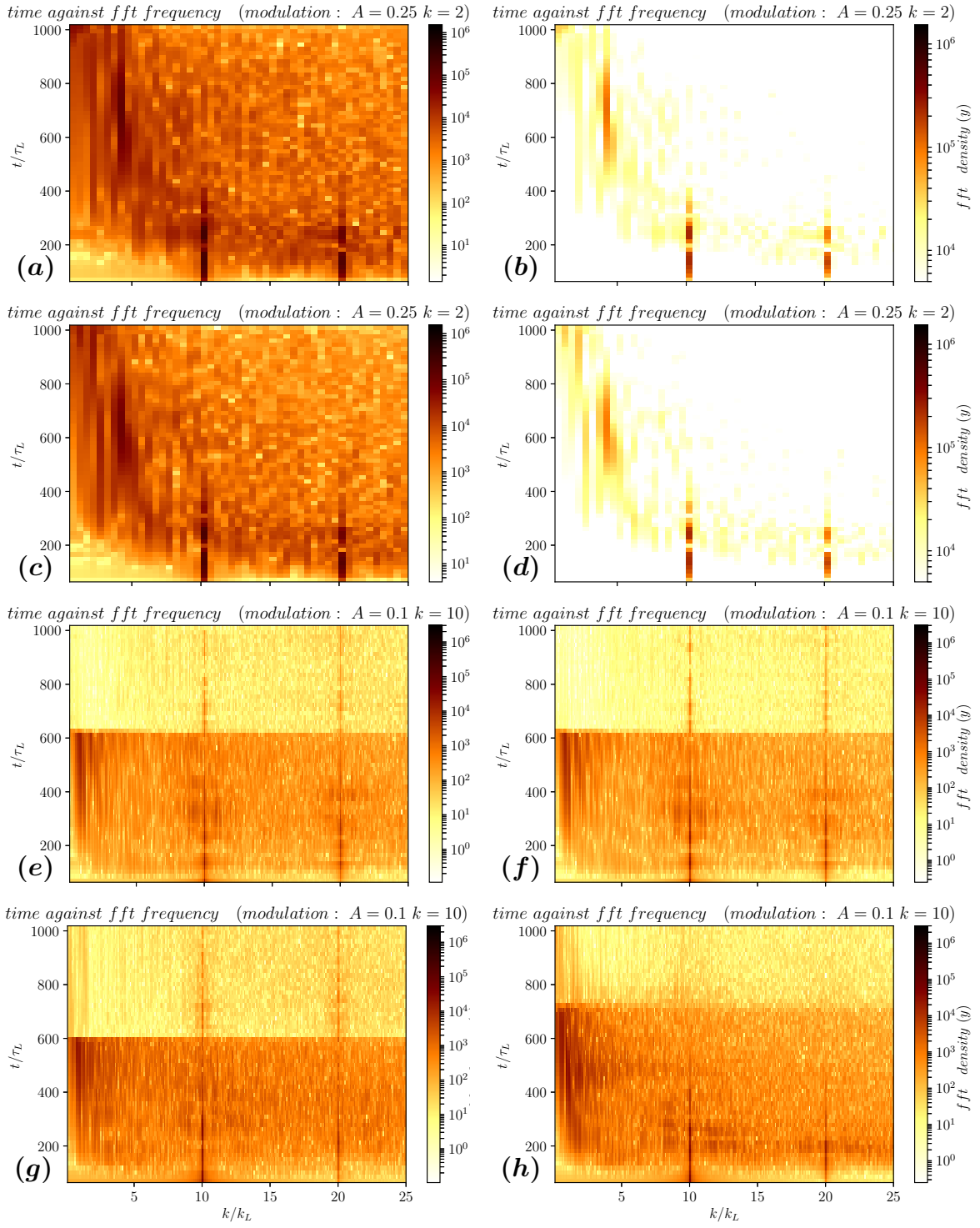

Figure 27: t/τ_L against k/k_L and $a_m = 0.25, k_m = 2$, with rpg modulation ($a_0 = 250$) for **(a)** the whole density behaviour, **(b)** selected density, ($a_0 = 150$) **(c)** the whole density behaviour, **(d)** selected density, $a_m = 0.10, k_m = 10$ with dm modulation for $1\lambda_0$ width **(e)** $a_0 = 250$, **(f)** $a_0 = 150$ (same for **(g)** and **(h)** with $2\lambda_0$ width).

5.2 Analyzing new finding in the RPA of ions for modulated targets

In the beginning, the density modulated target shapes were not supposed to be studied in this thesis as theory did not consider modulations in x-direction. However, accidentally, while creating different shapes of the targets we found the higher energy gains for density modulated targets. For density modulated targets, one could see a RPA-TNSA hybrid regime which is time dependent, *i.e* unstable in time. However, these new target shapes showed better results than the surface modulated target shapes and should be more studied in-depth.

In addition, some new physical trends were encountered in our simulation data in terms of ion density behaviour: one could see negative momentum of the ions, which led us into investigating the ion density evolution further. As previously stated, this behaviour could be explained by a loss of ions explained in section 3.2.3 (before figure Fig.20). The density in logarithmic scale are displayed in figure 28. Notice, that the logarithmic scale is important here (and was only chosen after observing the negative momentum area in the other figures), as without it, the density of the ions will look like a regular foil. The different behaviours in figure 28 are dependent on the modulation chosen and suggests of vortex formation and acceleration of ions due to it. The black transversal line should be the layer *i.e* area where the ions are accelerated by the constant laser pulse. However, the ions on the left side of the target are still moving in the other direction if we compare it with later time steps.

In order to understand these new effects better, one should investigate them further. They will probably lead to a new research direction which has not been explored yet.

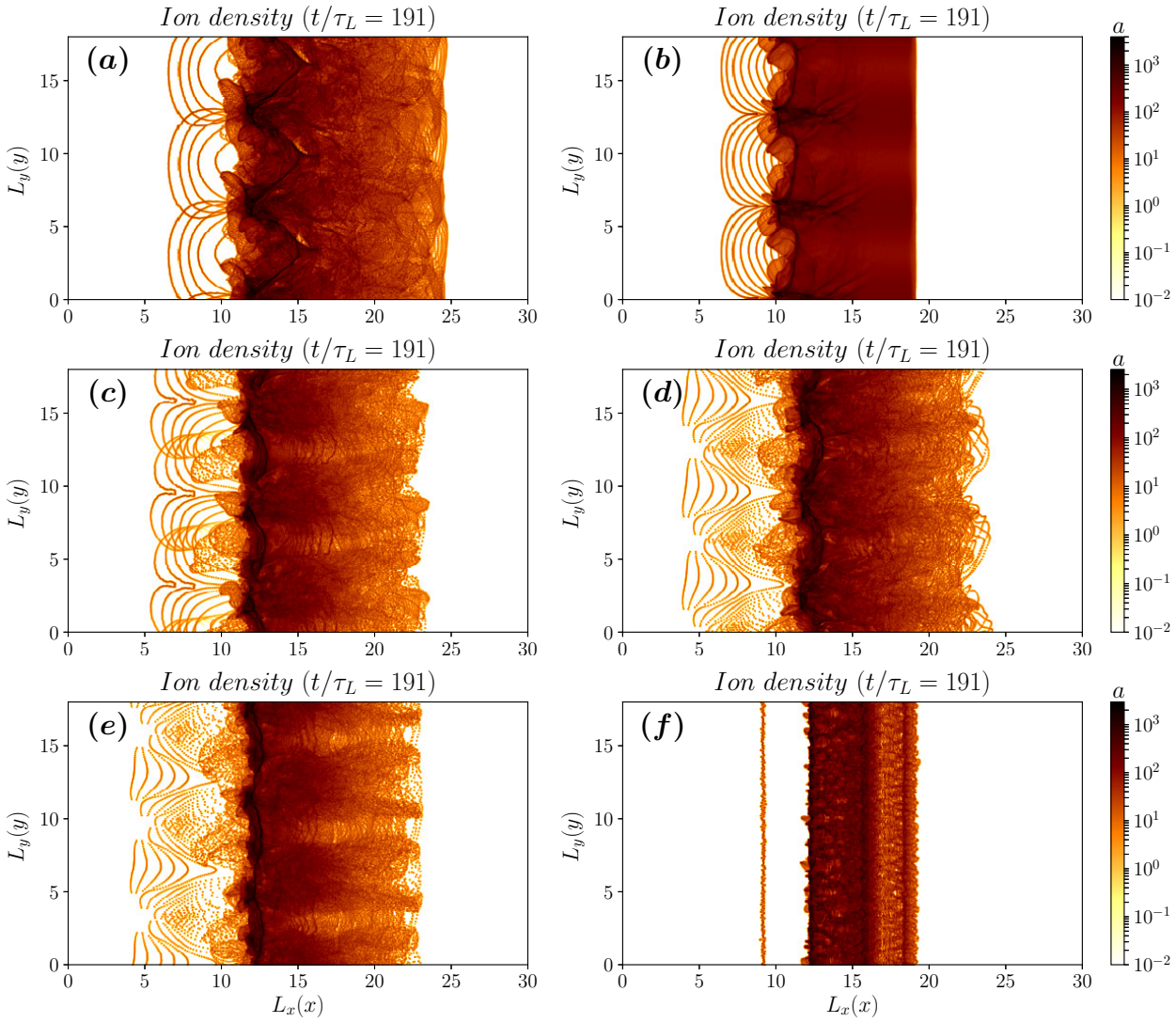

Figure 28: ion density behaviour for $t/\tau_L = 191$ with $a = n_0/n_c$, leading to a new research area, with **(a)** the density modulated target ($1\lambda_0$ width), **(b)** the density modulated target ($2\lambda_0$ width), **(c)** the rec surface-modulated target, **(d)** the rpg surface-modulated target, **(e)** the rp surface-modulated target and **(f)** the non-modulated target. All modulations are displayed for parameters $a_m = 0.5, k_m = 1$.

References

[1] René Heller and Michael Hippke, The Astrophysical Journal Letters 835, Vol. 2, L32 (6pp) (2017);

[2] T. Esirkepov, M. Borghesi, S. V. Bulanov, G. Mourou, and T. Tajima, Physical Review Letters 92, 175003 (2004);

[3] V. Malka, S. Fritzler, E. Lefebvre, E. d'Humieres, R. Ferrand, G. Grillon, C. Albaret, S. Meyroneinc, J. P. Chambaret, A. Antonetti, and D. Hulin, Med. Phys. 31, 1587 (2004);

[4] S. V. Bulanov, T. Z. Esirkepov, V. S. Khoroshkov, A. V. Kunetsov, and F. Pegoraro, Phys. Lett. A 299, 240 (2002);

[5] M. Borghesi, S. Bulanov, D. H. Campbell, R. J. Clarke, T. Z. Esirkepov, M. Galimberti, L. A. Gizzi, A. J. MacKinnon, N. M. Naumova, F. Pegoraro, H. Ruhl, A. Schiavi, and O. Willi, Phys. Rev. Lett. 88, 135002 (2002);

[6] A. J. Mackinnon, P. K. Patel, M. Borghesi, R. C. Clarke, R. R. Freeman, H. Habara, S. P. Hatchett, D. Hey, D. G. Hicks, S. Kar, M. H. Key, J. A. King, K. Lancaster, D. Neely, A. Nikkro, P. A. Norreys, M. M. Notley, T. W. Phillips, L. Romagnani, R. A. Snavely, R. B. Stephens, and R. P. J. Town, Phys. Rev. Lett. 97, 045001 (2006);

[7] C. K. Li, F. H. Seguin, J. A. Frenje, J. R. Rygg, R. D. Petrasso, R. P. J. Town, P. A. Amendt, S. P. Hatchett, O. L. Landen, A. J. Mackinnon, P. K. Patel, V. A. Smalyuk, T. C. Sangster, and J. P. Knauer, Phys. Rev. Lett. 97, 135003 (2006);

[8] S.V. Bulanov et al., Laser ion acceleration for hadron therapy, Phys.-Usp.57(2014) 1149;

[9] U. Linz and J. Alonso, Laser-driven ion accelerators for tumor therapy revisited, Phys. Rev. Accel. Beams19 (2016) 124802;

[10] P. Lalousis, I.B. Földes and H. Hora, in *Laser and Particle Beams* (2012), Vol. 30, pp. 233-242;

[11] V. Y. Bychekov, W. Rozmus, A. Maksimchuk, D. Umstadter, and C. E. Capjack, Plasma Phys. Rep. 27, 1017 (2001);

[12] M. Roth, T. E. Cowan, M. H. Key, S. P. Hatchett, C. Brown, W. Fountain, J. Johnson, D. M. Pennington, R. A. Snavely, S. C. Wilks, K. Yasuike, H. Ruhl, P. Pegoraro, S. V. Bulanov, E. M. Campbell, M. D. Perry, and H. Powell, Phys. Rev. Lett. 86, 436 (2001);

[13] S. Atzeni, M. Temporal, and J. J. Honrubia, Nucl. Fusion 42, L1 (2002);

[14] Y. Wan, C.-H. Pai, C. J. Zhang, F. Li, Y. P. Wu, J. F. Hua, W. Lu, C. Joshi, W. B. Mori, and V. Malka, Phys. Rev. E 98, 013202 (2018);

[15] F. Pegoraro and S. V. Bulanov Phys. Rev. Lett. 99, 065002 (2007);

[16] A. Sgattoni, S. Sinigardi, L. Fedeli, F. Pegoraro, and A. Macchi Phys. Rev. E 91, 013106 (2015);

[17] Min Chen, Naveen Kumar, Alexander Pukhov and Tong-Pu Yu Phys. of Plasmas 18, 073106 (2011);

[18] O. Klimo, J. Psikal, J. Limpouch and V.T.Tikhonchuk Phys. Rev. S.T - Acc. Beams 11, 031301 (2008);

[19] A. Einstein, Ann. Phys. (Leipzig) 322, 891 (1905);

6 Appendix

The density profile for the rectangular groove modulated target looks like:

```
trap1 = trapezoidal(n0,xvacuum=l0-am,xplateau=2*l0,xslope2=0.0)

def denProfile(x,y):
  if l0+am >= x >= l0-am:
    return trap1(x,y)*(am*math.cos(km*y)-am)
  if l0+am < x <= 2*l0:
    return n0
  if not (l0+am >= x >= l0-am and l0+am < x <= 2*l0):
    return 0.
```

The density profile for the rp modulated target looks like:

```
def denProfile(x,y):
  if l0+am >= x >= l0-am*math.cos(km*y):
    return n0
  if l0+am<x<=2*l0:
    return n0
  if not ((l0+am >= x >= l0-am*math.cos(km*y)) and (l0+am<x<=2*l0)
                                    ):
    return 0.
```

The density profile for the rpg modulated target looks like:

```
trap1 = trapezoidal(n0,xvacuum=l0-am,xplateau=2*l0,xslope2=0.0)

def denProfile(x,y):
  if l0+am >= x >= l0+am*math.cos(km*y):
```

```
    return trap1(x,y)*(am*math.cos(km*y)-am)
  if l0+am<x<=2*l0:
    return n0
  if not (l0+am >= x >= l0-am+am*math.cos(km*y) and (l0+am<x<=2*l0
                                    )):
    return 0.
```

The density profile for the density modulated target ($1\lambda_0$-width) looks like:

```
trap = trapezoidal(n0,xvacuum=l0,xplateau=2*l0,xslope2=0.0)

def denProfile(x,y):
  if ( 1.0*l0 < x < 3.*l0):
    return (0.5*am(3.0+math.cos(km*y)))*trap(x,y)
  else:
    return 0.
```

where `trapezoidal` is a smilei-implemented function

The python code for selecting the best energy spectrum of the sharpest peak:

```
path = "path/to/file"

# after looking into the area where the peak might be, the
                                  starting and ending time step are
                                  written here:
timestep_s = int(1322*2*math.pi)
timestep_e = int(1324*2*math.pi)

weight = 4.9*10**15
```

```
# open Smilei results
S = happi.Open(path, verbose=False)

# Parameters
dt = S.namelist.Main.timestep
dx = S.namelist.Main.cell_length[0]
dy = S.namelist.Main.cell_length[1]
simulation_time = S.namelist.Main.simulation_time

print ' Space steps:',dx,dy

t=int(simulation_time/dt)

#initial empty lists before filling
mx=[]
max_x=[]
fwhm=[]
tc=[]
root1 = []
root2 = []
hm=[]

for timestep in range(timestep_s,timestep_e):
  tc.append(timestep)
  PartDiag = S.ParticleBinning(diagNumber=0,timesteps = timestep)
  ekin = np.array(PartDiag.get()["ekin"])
  n = np.array(PartDiag.get()["data"][0])

#amplitude of the peak:
mx.append(np.max(n))
#mu_s1:
max_x.append(ekin[n.argmax()])
```

```
#calculating fwhm:
half_max = np.amax(n)/2.0
hm.append(half_max)
s = splrep(ekin, n - half_max, k=3)
roots = sproot(s)
# here one have to find the best roots
try:
  if roots[0]<ekin[n.argmax()]<roots[1]:
    fwhm.append(np.abs(roots[1]-roots[0]))
    root1.append(roots[0])
    root2.append(roots[1])
  elif roots[1]<ekin[n.argmax()]<roots[2]:
    fwhm.append(np.abs(roots[2]-roots[1]))
    root1.append(roots[1])
    root2.append(roots[2])
  else:
    fwhm.append(np.abs(roots[3]-roots[2]))
    root1.append(roots[2])
    root2.append(roots[3])
  except IndexError:
    fwhm.append(np.nan)

#converting the lists into arrays for further calculations:
hm = np.array(hm)
mx = np.array(mx)
tc = np.array(tc)/(2*math.pi)
de = np.array(fwhm)
e = np.array(max_x)
root1 = np.array(root1)
root2 = np.array(root2)

de_e = de/e
```

```
xs_de_e = 0
ti = timestep_s
nan = np.nan

# Here the best time step will be searched before plotting
def find_ti(de_e,e):
  xs_de_e = 0
  ti = 0
  for i in range(0,len(de_e)):
    if (xs_de_e < de_e[i]) and xs_de_e!=0:
      xs_de_e = xs_de_e
    else:
      xs_de_e = de_e[i]
      ti = i
  return ti+timestep_s

# ion energy spectrum is then plotted
```

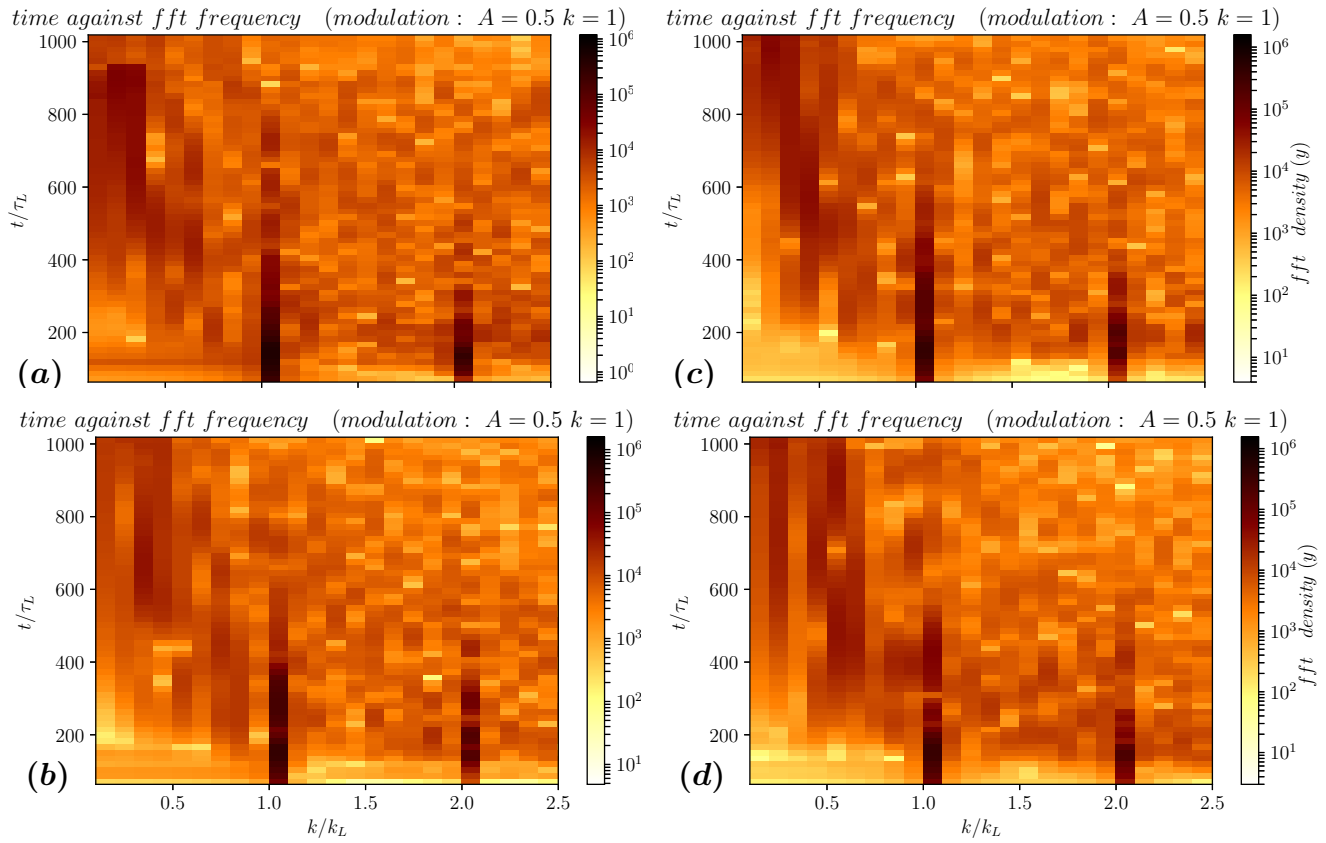

Figure 29: time *i.e* t/τ_L against FFT of the frequency, defined as the normalized wave vector k/k_L with the whole density behaviour in third dimension and $a_m = 0.50, k_m = 1$ for **(*a*)** the density modulated target ($1\lambda_0$ width), **(*b*)** the rp surface-modulated target, **(*c*)** the rec surface-modulated target and **(*d*)** the rpg surface-modulated target.

List of Figures

Erklärung

Ich versichere, dass ich diese Arbeit selbstständig verfasst und keine anderen als die angegebenen Quellen und Hilfsmittel benutzt habe.

Heidelberg, den 9. September 2019,